# Search for Massive Randall-Sundrum Graviton Excitations in the CMS Experiment at the LHC

Piotr Traczyk

Department of High-Energy Physics

Soltan Institute for Nuclear Studies

*A thesis submitted in partial fulfillment of the requirements for the degree of Doctor of Philosophy in Physics*

*Supervised by dr hab. Grzegorz Wrochna*

Warsaw, 2006

# Acknowledgements

I am most grateful to my supervisor dr hab. Grzegorz Wrochna for many valuable suggestions and guidance throughout the course of preparing this thesis.

I would like to thank the members of the Warsaw CMS group for countless discussions, and a friendly atmosphere.

I would like to thank Bob Cousins from the UCLA CMS group for many helpful discussions, also Maria Spiropulu and Luc Pape, the heads of the CMS SUSY/BSM (Beyond the Standard Model) group, for their support and encouragement.

I would also like to thank Włodzimierz Natorf, my high school physics teacher for springing my interest in physics and giving me a solid base for future development.

Finally I would like to thank my wife, family and friends for their support and patience.

# Abstract

In this thesis a study of the possibility of observing Randall-Sundrum graviton resonances through their dimuon decay mode in the CMS detector at the LHC is presented. The analysis was performed on Monte Carlo data with full detector simulation and reconstruction. The results show that it is possible to discover the Randall-Sundrum graviton at $5\sigma$ level in the whole theoretically allowed region of parameter space, after collecting 100 $\text{fb}^{-1}$ of data. The reach of the experiment in graviton mass is estimated at 1.7-4.4 TeV, depending on the graviton coupling. The possibility to distinguish the newly discovered particle from a spin-1 $Z'$ state was also studied, and $2\sigma$ exclusion is expected for graviton masses up to 1-1.5 TeV for low coupling and 2.6-2.9 TeV for high coupling, depending on the method used.

# Contents


**1 Introduction** **1**

1.1 Extra dimensions in physics . . . . . 2

1.1.1 Theory of relativity . . . . . 2

1.1.2 The Kaluza-Klein theory . . . . . 3

1.1.3 String theory . . . . . 4

1.2 Modern theories with extra dimensions . . . . . 4

1.2.1 The ADD model . . . . . 5

1.2.2 The Randall-Sundrum model . . . . . 7

1.3 Overview of the studied channel . . . . . 8

1.3.1 The signal process $pp \to G^* \to \mu\mu$ . . . . . 10

1.3.2 Background . . . . . 11

1.4 Analysis overview . . . . . 12

**2 The CMS Experiment** **13**

2.1 The LHC collider . . . . . 13

2.2 CMS Detector Overview . . . . . 15

2.3 The Muon System . . . . . 16

2.3.1 Overview . . . . . 16

2.3.2 Drift Tubes (DT) . . . . . 18

2.3.3 Cathode Strip Chambers (CSC) . . . . . 20

2.3.4 Resistive Plate Chambers (RPC) . . . . . 21

2.4 Inner Tracker . . . . . 23

2.5 Calorimetry . . . . . 24

2.5.1 Electromagnetic calorimeter (ECAL) . . . . . 24

2.5.2 Hadronic calorimeter (HCAL) . . . . . 25

2.6 Summary of detector performance . . . . . 26
2.7 The Trigger . . . . . 27

**3 Signal generation, detector simulation and reconstruction 30**
3.1 Monte-Carlo sample generation . . . . . 31
3.1.1 Signal . . . . . 31
3.1.2 Background . . . . . 31
3.2 Muon reconstruction in CMS . . . . . 34
3.2.1 Local reconstruction in the muon detectors . . . . . 34
3.2.1.1 Drift Tubes . . . . . 34
3.2.1.2 Cathode Strip Chambers . . . . . 36
3.2.1.3 Resistive Plate Chambers . . . . . 37
3.2.2 Standalone muon reconstruction . . . . . 37
3.2.3 Global Muon reconstruction . . . . . 38
3.3 Custom offline improvements in muon reconstruction . . . . . 39
3.3.1 The Picky Muon Reconstructor . . . . . 41
3.3.2 Recovering bremsstrahlung photons . . . . . 46

**4 Analysis 50**
4.1 Method of discovering a TeV mass resonance . . . . . 50
4.1.1 Discovery significance estimators . . . . . 51
4.1.2 Toy Monte-Carlo tests of significance estimators . . . . . 55
4.2 Method of determining the spin of the observed particle . . . . . 58
4.3 Other methods of distinguishing between the G and the $Z'$ . . . . 62
4.4 Results . . . . . 65
4.4.1 $5\sigma$ Discovery reach . . . . . 65
4.4.2 Resonance mass measurement . . . . . 65
4.4.3 Establishing the identity of the observed particle . . . . . 69
4.5 Systematic uncertainties . . . . . 71
4.6 Conclusions . . . . . 73

**5 Summary 74**

**References 79**

# List of Figures


1.1 Theoretical and experimental constraints in the Randall-Sundrum model parameter space. . . . . 9
1.2 The leading order process for graviton production in a proton-proton collider. . . . . 11

2.1 Overview of the LHC accelerator ring and the detectors . . . . . 15
2.2 Overview of the Compact Muon Solenoid detector . . . . . 16
2.3 Longitudinal view of one quadrant of the CMS detector. . . . . 18
2.4 Transverse view of the CMS detector . . . . . 19
2.5 The principle of operation of a Cathode Strip Chamber. . . . . 21
2.6 The double gap layout of CMS Resistive Plate Chambers . . . . . 22
2.7 The CMS electromagnetic calorimeter . . . . . 25
2.8 Event rates and cross sections of selected processes for the LHC design luminosity of $10^{34} cm^{-2} s^{-1}$. . . . . 28

3.1 Invariant mass spectrum of the simulated Drell-Yan background. Different colors correspond to different $\hat{p_t}$ bins. . . . . 33
3.2 Reconstructed hits in a Drift Tube chamber. . . . . 36
3.3 CMS muon transverse momentum resolution for different values of muon momentum and pseudorapidity. . . . . 40
3.4 Efficiency of the CMS muon system for different values of muon momentum and pseudorapidity. . . . . 40
3.5 Cross sections for electron production by muons traversing matter. 42
3.6 CMS momentum reconstruction resolution for 1500 GeV muons. Comparison between GMR and PMR. . . . . 44

3.7 CMS momentum reconstruction resolution for 50 GeV muons. Comparison between GMR and PMR. . . . . 45
3.8 Reconstructed momentum of $p_t = 1000$ single muons, with and without brem photon correction. . . . . 46
3.9 Fraction of muon energy carried by the reconstructed photon and scatter-plot of photon momentum vs its distance from the corresponding muon. . . . . 47
3.10 Reconstructed photons in a 0.1 $\eta$-$\phi$ cone, from 3 TeV $G \to \mu\mu$ signal sample. . . . . 48
3.11 Reconstructed invariant mass spectrum of a $G \to \mu\mu$ signal sample. 49

4.1 Reconstructed invariant mass distribution for a pure signal sample, with the signal pdf fit overlayed. . . . . 53
4.2 Reconstructed invariant mass distribution for the Drell-Yan background process, with the background-only pdf fit overlayed. . . . . 54
4.3 Distributions of $S_L$ values obtained in fits to 10000 simulated pseudo-experiments. . . . . 56
4.4 Large statistics (10 million) toy Monte-Carlo test of $S_L$ behavior for a background-only data sample. . . . . 57
4.5 Theoretical angular distribution shapes for spin-1 and spin-2 resonances. . . . . 59
4.6 Angular distributions for 3000 GeV generated $Z'$ and graviton. . . 59
4.7 Contributions to the likelihood function from individual simulated events, for a 1000 GeV graviton and $Z'$, with the Drell-Yan contribution added. . . . . 61
4.8 Values of $-2\ln\lambda$ obtained in 10000 pseudo-experiments, for a 1000 GeV graviton and $Z'$. . . . . 62
4.9 Transverse momentum of the dimuon system for a 1 TeV graviton and $Z'$. . . . . 63
4.10 Two-dimensional plots of the dimuon $p_t$ and $cos\theta^*$ distributions for a 1000 GeV graviton and $Z'$. . . . . 64

4.11 Contributions to the 2D ($p_t$ and $cos\theta^*$) likelihood function from individual simulated events, for a 1000 GeV graviton and $Z'$, with the Drell-Yan contribution added. . . . . 64
4.12 Values of $-2\ln\lambda$ obtained in 10000 pseudo-experiments, for a 1000 GeV graviton and $Z'$. . . . . 65
4.13 CMS reach for $5\sigma$ discovery of the Randall-Sundrum graviton. . . 66
4.14 Reconstructed graviton mass distribution for a graviton with mass equal to 1500 GeV and $c = 0.01$. . . . . 67
4.15 Relative error on reconstructed graviton mass. . . . . 68
4.16 Relative precision of the graviton mass fit. . . . . 68
4.17 CMS reach for $2\sigma$ discrimination between spin-1 and spin-2 hypotheses for different integrated luminosities, based of angular distributions. . . . . 69
4.18 CMS reach for $2\sigma$ discrimination between a graviton and a $Z'$ for different integrated luminosities, with both angular and $p_T$ distributions used in the analysis. . . . . 70

# Chapter 1

# Introduction

The startup of the LHC is eagerly awaited by particle physicists, expecting to find answers to many important questions by probing a previously unexplored energy region. For example, there is hope of finding a trace of a more fundamental theory beyond the Standard Model. One of such scenarios is the model of Randall and Sundrum, introducing an extra spatial dimension and providing a solution for the gauge hierarchy problem. The model predicts the existence of heavy excitations of gravitons, which could be observed in a high energy collider. An analysis of the possibility to discover these new particles is presented in this thesis.

The thesis is divided into five chapters. The first chapter contains a brief overview of theories with extra dimensions, with a description of the recent models like ADD (Arkani-Hamed, Dimopoulos, Dvali) and RS (Randall, Sundrum). The LHC collider and CMS detector are described in the second chapter, with a focus on the CMS muon system.

The third chapter contains a description of the Monte-Carlo sample generation and detector simulation procedures. Muon reconstruction in CMS is described in detail, along with modifications made to the standard algorithms to improve the performance for high energy muons.

The analysis of the simulated data is described in Chapter 4. The methods for establishing the expected reach of the CMS experiment are presented, for discovery of a Randall-Sundrum graviton and for distinguishing between a graviton and a $Z'$ particle. The fifth chapter contains a summary.

## 1.1 Extra dimensions in physics

For many years, physicists have successfully been using flat three-dimensional space to provide a mathematical description for the world surrounding them. In the last hundred years, theories proposing a more complex geometrical description of Nature started to emerge. The first step was Einstein's Special and General Relativity, dealing with the geometry of 4-dimensional spacetime, and moving from flat to curved space. While revolutionary, these ideas didn't actually add any new spatial dimensions, since the fourth dimension was time. The idea of a fifth dimension first appeared in the theory of Kaluza and Klein nearly twenty years later, and in the 70's even more dimensions (10, 11 or even 26) were introduced in string theories. These were, however, of little interest form the experimentalist's point of view, since energies needed to probe their possible effects were of the order of $10^{19}$ GeV - far beyond the reach of any collider in any foreseeable future. The situation changed in the late 1990's with the introduction of the ADD model and subsequent theories incorporating extra dimensions, and at the same time predicting new phenomena at energies of the order of a TeV.

### 1.1.1 Theory of relativity

The Theory of Relativity was presented by Albert Einstein in 1905. It consists of two parts – Special Theory of Relativity (STR), dealing with objects and reference frames at rest or moving with constant speeds, and the introduced in 1916 General Theory of Relativity (GTR), dealing with dynamics, accelerating reference frames and gravity.

In STR, time is introduced as a new, fourth dimension. The notion to use four numbers to describe phenomena, representing their temporal, as well as spatial location, is not really new. What is new, however, is the interplay between space and time, with one transforming into the other when changing reference frames.

General relativity makes use of curved spacetime, providing a description of the gravitational force on a purely geometrical basis: energy and mass create a gravitational field, which is mathematically represented by spacetime curvature. Bodies freely traveling in straight lines in such curved space are pulled toward each other, just as two straight lines on a sphere have to eventually intersect.

Einstein's theory revolutionized the physicists' view of the world, predicting many new phenomena, that have later been observed in nature (gravitational lenses, black holes, time dilation etc.). The famous formula relating energy and mass, together with the kinematics of objects moving with speeds close to the speed of light, are the basis of modern physics.

### 1.1.2 The Kaluza-Klein theory

A few years after the publication of GTR, Theodor Kaluza tried solving Einstein's equations in five-dimensions. He discovered that what emerged was in fact the original description of gravity in four dimensions, plus Maxwell's equations of electrodynamics [1]. Such unexpected unification of gravity and electromagnetic interactions was a very exciting idea, but it faced a simple question - where is the fifth dimension? In 1926 Oskar Klein proposed a solution, introducing a mechanism known as compactification [2]. As opposed to the other four dimensions, the fifth one is finite in size, and "rolled down" into a small circle. With the circle's radius being sufficiently small, five-dimensional spacetime would appear to have only four dimensions.

Klein also estimated the size of the new dimension on the ground of quantum mechanics. A new dimension topologically equivalent to a circle imposes periodic boundary conditions on the wave function of a particle propagating in this dimension, resulting in a tower of discrete states. From the four-dimensional point of view, these states appear as particles with different electric charge. Klein calculated the compactification radius corresponding to the known value of the elementary charge, and obtained as a result a value of the order of $10^{-33}$ cm. This effectively rendered the theory useless, since there was no way to probe experimentally such small distances and test whether such fifth dimension exists. Physicists lost interest in the theory, and turned study the emerging theory of quantum mechanics, which, in contrast, had spectacular success in predicting and explaining the outcome of many experiments.

### 1.1.3 String theory

String theory introduced even more dimensions in a framework giving hopes of unifying all interactions. It can be traced back to 1968, when Veneziano constructed a theory using Euler's beta function to describe hadron scattering [3]. This theory was identified as a theory of relativistic vibrating strings by Nambu [4] and Goto (1970). But new experimental data disagreed with the model's predictions for strong interactions, for example the theory predicted spin-2 states which were not observed in experiments.

These spin-2 states were reinterpreted as gravitons in 1974, when Schwarz and Yoneya changed the scope of the theory from 1 GeV to $10^{19}$ GeV [5],[6]. Requirements of Lorentz invariance and unitarity led to a formulation of bosonic string theory that was consistent only in 26 dimensions. Adding fermions to the theory required the introduction of supersymmetry - a new symmetry exchanging bosons with fermions.

Studies of supersymmetric string theories (superstring theories) resulted in mid-1980's in the formulation of five 10-dimensional string theories in - Type I, Type IIA and IIB, $SO(32)$ heterotic and $E_8 \times E_8$ heterotic. 10 years later these were found to be equivalent to one another through so-called *dualities*, and are now believed to be five incarnations of an even more fundamental, 11-dimensional M-theory. The exact formulation of this theory is, however, unknown.

While many theorists believe that string (or M-) theory might be *The* theory unifying all fundamental interactions, there is currently no way of testing it experimentally. There are still many degrees of freedom, like the choice of quantum vacuum or compactification scheme, leading to an arbitrarily large number of models, all in agreement with current experimental data [7].

## 1.2 Modern theories with extra dimensions

In the late 1990's new theories involving extra dimensions have been proposed. As opposed to string theories, these models gave experimental predictions that could be studied in colliders and other experiments. They all emerged as solutions to the gauge hierarchy problem - the puzzle of the weakness of gravity compared to the

other three fundamental forces. The energy scale of gravity, given as the inverse of the Newton's constant, is the Planck mass, $M_{Pl} \simeq 10^{19}$ GeV. The energy scale of electroweak interactions, $M_{EW}$ is of the order of $10^3$ GeV. The existence of two such different fundamental energy scales is very unnatural, for example if the Standard Model would be valid up to $M_{Pl}$, a very delicate fine-tuning would be required to keep the square of the Higgs boson mass stable against quantum loop corrections.

### 1.2.1 The ADD model

One of the first solutions of the hierarchy problem involving extra spatial dimensions was the model proposed in 1998 by Arkani-Hamed, Dimopoulos and Dvali (ADD)[8]. It is based around the observation that, while the electroweak scale has been tested at distances of the order of $1/M_{EW}$, the gravitational force is far from being explored at distances of $1/M_{Pl} \sim 10^{-33}$ cm. At the time the article was published, Newton's law was tested at $\sim$1 cm distances. In conclusion, if $M_{Pl}$ is really a fundamental scale in nature, gravity must stay unmodified over the 33 orders of magnitude from 1 cm down to $10^{-33}$ cm.

This reasoning leads the authors to the idea of abandoning the interpretation of $M_{Pl}$ as a fundamental energy scale, and leaving only one fundamental scale – $M_{EW}$. To account for the observed weakness of gravity (compared to electroweak interactions), new spatial dimensions are introduced, with gravity being the only fundamental interaction that "sees" them. The Standard Model fields are trapped on a 4-dimensional wall (often called a "brane") in the extra dimensions, and gravitons are the only particles freely propagating in the whole space (the "bulk"). In the case of $n$ extra dimensions with a common compactification radius of $R$, one can calculate the gravitational potential for two test masses $m_1$ and $m_2$ placed at a distance $r \ll R$ writing Gauss' law in $(4+n)$ dimensions

$$V(r) \sim \frac{m_1 m_2}{M_{Pl(4+n)}^{n+2}} \frac{1}{r^{n+1}} \tag{1.1}$$

where $M_{Pl(4+n)}$ is the fundamental scale of gravity in the extra dimensions, and is assumed to be of the order of $M_{EW}$. When the test masses are moved away to a distance much larger that the compactification radius $r \gg R$, the gravitational

flux lines no longer propagate in the extra dimensions and the potential returns to the familiar $1/r$ form,

$$V(r) \sim \frac{m_1 m_2}{M_{Pl(4+n)}^{n+2} R^n} \frac{1}{r} \tag{1.2}$$

Comparing 1.1 and 1.2 yields the relation

$$M_{Pl(4+n)}^{n+2} R^n = M_{Pl} \tag{1.3}$$

The observed strength of gravity can be reproduced with a suitable choice of $R$ and $n$, such that

$$R \sim 10^{\frac{30}{n}-17} cm \times (\frac{1TeV}{M_{EW}})^{1+\frac{2}{n}} \tag{1.4}$$

The case with $n = 1$ corresponds to $R \sim 10^{13}$ cm, which would imply deviations from Newton's law at distances on the scale of the Solar System[1], at which it is well established. Hence the number of extra dimensions must be larger. For $n = 2$ the value of $R$ is $\sim$1 mm, and this is now also excluded. Current limits on the size of extra dimensions from precision tests of the gravitational force are of the order of 200 $\mu$m [9]. Higher numbers of extra dimensions, up to the 10 or 11 suggested by string theory, predict deviations at smaller distances, and are not excluded by gravitational measurements.

In the ADD framework the graviton couples to other particles with a strength $\sim 1/M_{Pl}$, but since it can propagate into the extra dimensions, it can also have momentum in the new dimension. From the 4-dimensional point of view, such momentum appears as mass, and is quantized. A whole tower of Kaluza-Klein excited states with masses separated by $1/R$ appears. Calculating the cross-section of a TeV scale physics process requires summing over all the states with masses smaller that the energy available to the graviton. Due to the sheer multiplicity of these states, the cross-section can be of the order of electroweak cross-sections. This way the ADD model predicts effects that can be studied in collider experiments.

[1] $10^{13}$ cm = $10^8$ km, the Earth's orbit has a radius of $\sim 1.5 \times 10^8$ km

### 1.2.2 The Randall-Sundrum model

A closer look at the geometric solution for the hierarchy problem proposed by ADD reveals one flaw: the discrepancy between $M_{Pl}$ and $M_{EW}$ is not really removed, it is moved elsewhere. A result of compactifying the extra dimensions on a circle with a radius of $R$ is a new hierarchy between the electroweak scale, and the compactification scale $1/R$. This inspired a different approach, proposed by Randall and Sundrum [10], with only one extra dimensions and non-trivial geometry.

The authors propose a set-up with the extra dimension, denoted by $0 < \phi < 2\pi$, which is compactified on an orbifold[1]. The two fixed points of the orbifold, $\phi = 0, \pi$, hold two 3-branes. The solution to Einstein's equations in such 5-dimensional space is an anti-de Sitter ($AdS_5$) space with non-factorizable geometry, given by the metric

$$ds^2 = e^{-2kr_c\phi}\eta_{\mu\nu}dx^\mu dx^\nu + r_c^2 d\phi^2 \tag{1.5}$$

where $k \sim M_{Pl}$ is the $AdS_5$ curvature parameter, $r_c$ is the compactification radius, $x^\mu$ are the standard 4-dimensional coordinates and $\eta_{\mu\nu}$ is the 4-dimensional metric tensor. Assuming that the SM fields are confined to the brane located at $\phi = \pi$, any fundamental, 5-dimensional mass parameter $m_0$, has an effective 4-dimensional value of

$$m = e^{-kr_c\pi}m_0 \tag{1.6}$$

This way TeV masses can be easily generated from parameters of order of the Planck scale, by choosing $kr_c \sim 11 - 12$. The compactification scale $1/r_c$ is of the order of $M_{Pl}$, so no additional hierarchy is introduced.

Kaluza-Klein (KK) graviton excitations in this model have significantly different properties than in the case with large extra dimensions. The interactions of matter fields with the graviton tower are given by the Lagrangian [11]

$$L = -\frac{1}{M_{Pl}}T^{\alpha\beta}h^{(0)}_{\alpha\beta} - \frac{1}{\Lambda_\pi}T^{\alpha\beta}\sum_{n=1}^{\infty}h^{(n)}_{\alpha\beta} \tag{1.7}$$

[1] An orbifold is a circle with an additional condition $(x, \phi) = (x, -\phi)$ imposed.

where $h_{\mu\nu}$ are the graviton fields, $T^{\alpha\beta}$ is the energy-momentum tensor of the matter field, and $\Lambda_\pi$ is the coupling parameter, given by

$$\Lambda_\pi = M_{Pl} e^{-kr_c\pi} \tag{1.8}$$

and is of order of the weak scale.

As can be seen from the Lagrangian, while the massless zero-mode of the graviton couples with the usual $1/M_{Pl}$ strength, the coupling of the KK excitations, determined by the $\Lambda_\pi$ parameter, is comparable to $1/M_{EW}$. The masses of the KK modes are

$$m_n = k x_n e^{-kr_c\pi} \tag{1.9}$$

where $x_n$ is the n-th root of the $J_1$ Bessel function. Such KK gravitons would show up in collider experiments as individual resonances, providing a good way of testing the model.

The Randall-Sundrum model phenomenology is governed by two free parameters, with the mass of the first graviton excitation $m_1$ and the ratio $c = k/M_{Pl}$ being the usual choice [11]. The parameter space is strongly constrained, both by experimental data from LEP and Tevatron and by theoretical limits, shown in Fig. 1.1. The $c < 0.1$ boundary is a limit on the curvature of the bulk space, further motivated by string-theoretical arguments [12]. It is complimented by a somewhat arbitrary bound of $\Lambda_\pi < 10$ TeV, added to ensure that no new hierarchy is introduced in the model. The resulting allowed region is a closed area in the parameter space, as can be seen from Fig. 1.1.

## 1.3 Overview of the studied channel

In this work, evidence for the existence of a warped extra dimension will be searched for in high energy proton-proton collisions in the LHC collider. A center-of-mass energy of 14 TeV allows for direct production of heavy graviton resonances, which could be discovered through the observation of their decay products in the CMS detector.

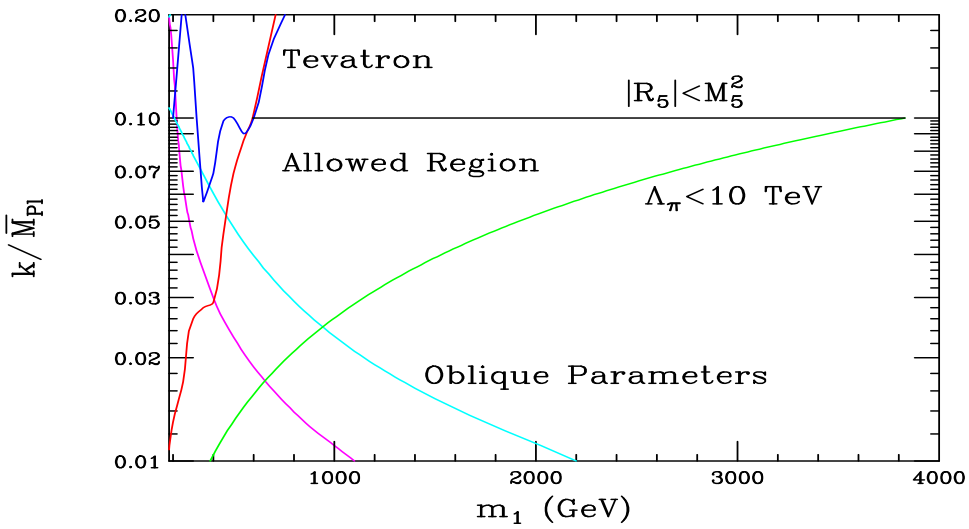


Figure 1.1: Theoretical and experimental constraints in the Randall-Sundrum model parameter space [12]. The purple and cyan curves represent lower bounds from fits to electroweak oblique parameters (T and S, respectively), the blue and red curves mark the region excluded by Tevatron dijet and dilepton searches. The black and yellow curves represent theoretical upper bounds.

The Randall-Sundrum graviton can decay into all Standard Model particles, branching fractions for a 1 TeV graviton are shown in Table 1.1. Leptonic decays provide a promising discovery channel - electrons or muons can be directly observed in detectors, and the background is expected to be small. This is different in the case of hadronic decays which, although providing a higher cross-section because of a larger branching fraction, result in final states with jets, with a relatively high QCD background and larger experimental uncertainties. The channel with two photons in the final state is, on the other hand, a good candidate for a discovery channel [13]. Prompt photon background is very low, and the branching fraction is large. Decays into W or Z boson pairs provide supplementary detection channels with more complex final state topologies, with combinations of leptons jets and missing energy [14].

Preliminary studies of the dilepton and diphoton channel observability in the CMS experiment have already been made [16], with fast, parameterization-based simulation of detector response, CMSJET [17]. The conclusion from these studies is that the whole interesting region in the parameter space of the Randall-Sundrum model should be accessible to the CMS detector after collecting 100 $fb^{-1}$

| Decay channel | Branching ratio |
|---|---|
| $d + \bar{d}$ | 6.29% |
| $u + \bar{u}$ | 6.29% |
| $s + \bar{s}$ | 6.29% |
| $c + \bar{c}$ | 6.29% |
| $b + \bar{b}$ | 6.29% |
| $t + \bar{t}$ | 6.22% |
| $e^- + e^+$ | 2.04% |
| $\nu_e + \bar{\nu_e}$ | 2.04% |
| $\mu^- + \mu^+$ | 2.04% |
| $\nu_\mu + \bar{\nu_\mu}$ | 2.04% |
| $\tau^- + \tau^+$ | 2.04% |
| $\nu_\tau + \bar{\nu_\tau}$ | 2.04% |
| g + g | 32.69% |
| $\gamma + \gamma$ | 4.09% |
| $Z^0 + Z^0$ | 4.44% |
| $W^+ + W^-$ | 8.87% |

Table 1.1: Branching ratios for different graviton decay processes, calculated by Pythia [15].

of data[1]. In this work a detailed analysis of the dimuon decay mode is described, with detailed detector simulation (including dedicated studies of high energy muon reconstruction).

### 1.3.1 The signal process $pp \to G^* \to \mu\mu$

Two tree-level diagrams contribute to the $pp \to$ G process: quark-quark annihilation and gluon-gluon fusion (see Fig. 1.2). The relative contribution of these subprocesses changes with the graviton mass, from $qq$:$gg$ ~1:6 for 1 TeV gravitons to $qq$:$gg$ ~2:1 for 4 TeV resonances. The experimental signature of this process is a pair of very energetic, opposite sign muons, with invariant mass close to the mass of the graviton.

[1] this corresponds to one year of LHC running with the design luminosity.

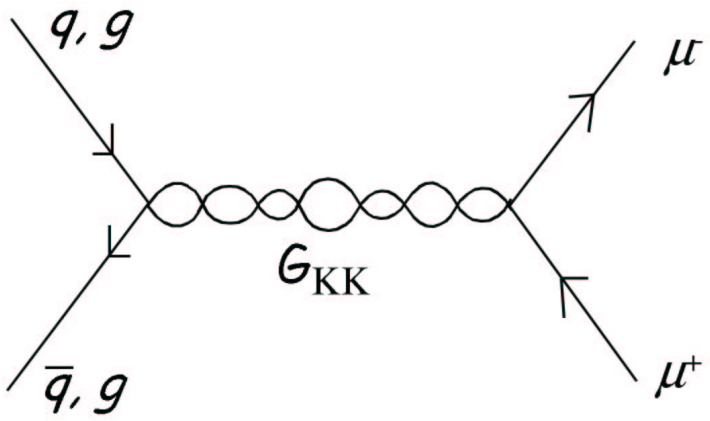


Figure 1.2: The leading order process for graviton production in a proton-proton collider.

### 1.3.2 Background

The main and irreducible background for the signal process considered is the Drell-Yan process [18], in which a pair of quarks from the colliding protons produces a virtual $Z^0$ boson or a photon, which then decays to two leptons. In this energy region relevant for this analysis (where the mass of the exchanged particle is of the order of the graviton mass) the cross section as a function of the exchanged resonance's mass is governed by the availability of partons in the colliding protons with momenta high enough to produce such a particle, described by the parton distribution functions (pdf's) of the proton.

Other SM processes can also yield a muon pair in the final state. These include semileptonic decays of heavy quark pairs $t\bar{t}$ and $b\bar{b}$, and W and Z boson pair production. Dimuon rates from these backgrounds are about one order of magnitude smaller than the rate from the Drell-Yan process. Furthermore, they can be additionally reduced by requiring that the muons are isolated and there is no missing transverse momentum in the event. Because of this, Drell-Yan dimuon production is the only background process considered in this analysis.

Another possible source of high energy dimuons is event pileup. A single bunch crossing will produce an average of 3.5 inelastic proton-proton collisions at low luminosity ($10^{33} cm^{-2} s^{-1}$) or 17.5 at high luminosity ($10^{34} cm^{-2} s^{-1}$). This is not an important source of background in this analysis since the rate of single

muons from pileup is expected to be falling fast with muon momentum - an event with two very energetic muons, both originating from pileup, is highly unlikely.

When searching for new physics in a yet-unexplored energy region, one has to take into account the possibility of other background sources besides SM processes. The main candidate for such background is a heavy vector boson, generically called a $Z'$ - an extra neutral gauge boson appearing in various extensions of the Standard Model (Grand Unified Theories [19], extra dimensions [20], string theory [21], Little Higgs [22] etc.). This particle doesn't really contribute as a background process, but rather provides an alternative signal signature. Hence, a discovery of a new heavy particle has to be followed by a more detailed study to determine it's theoretical origin.

## 1.4 Analysis overview

The analysis consists of two main parts, focusing on discovering an excited graviton and on distinguishing it from a $Z'$. The search for a signal is done in the dimuon invariant mass spectrum, where the graviton shows up as an accumulation of events around it's mass value, visible as a peak on top of the exponentially falling Drell-Yan continuum. Checking whether the observed particle is really a graviton is done mainly by analyzing the angular distributions of the muons. Since the $Z'$ particles have spin 1 (as opposed to the graviton, having spin 2), angular distributions of the resonance's decay products can be used to distinguish between the two, as is shown in Section 4.2.

# Chapter 2

# The CMS Experiment

## 2.1 The LHC collider

The year 2000 was the last year of running of the Large Electron Positron collider (LEP), in which electron and positron beams with energies reaching 105 GeV were collided. Particles were accelerated in a circular, 26.7 km long underground tunnel in the European Laboratory for Particle Physics (CERN), located near Geneva in Switzerland. This tunnel will now house the Large Hadron Collider (LHC) [23], a machine designed to produce collisions of proton beams, with each beam having an energy of 7 TeV. The center-of-mass energy that will be available in the LHC is thus 14 TeV. The existing CERN infrastructure, with some minor modifications, will be used for injecting the protons into LHC (Linac, Booster, Proton Synchrotron (PS), Super Proton Synchrotron (SPS)). The SPS accelerates protons to an energy of 450 GeV, and the remaining acceleration is done by the LHC during the first 20 minutes after beam injections.

The protons travel around the accelerator ring in bunches, with each bunch consisting of $\sim 10^{11}$ protons. The spacing between bunches is 7.5 m, or 25 ns, corresponding to a 40 MHz rate of bunch collisions at the interaction points, where particle detectors are located. The design luminosity for LHC is $10^{34} cm^{-2} s^{-1}$. A summary of the main parameters of the accelerator is shown in Table 2.1.

Six experiments are planned to run on the LHC - two general-purpose detectors:

- ATLAS (A Toroidal LHC ApparatuS),

| | | |
|---|---|---|
| Beam energy | [TeV] | 7.0 |
| Dipole field | [T] | 8.4 |
| Luminosity | [$cm^{-2}s^{-1}$] | $10^{34}$ |
| Injection energy | [GeV] | 450 |
| Bunch spacing | [ns] | 24.95 |
| Number of bunches | | 2835 |
| Particles per bunch | | $1.05 \times 10^{11}$ |
| r.m.s. bunch length | [m] | 0.075 |
| Full crossing angle | [$\mu$rad] | 200 |
| Number of events per crossing | | 19 |
| Circulating current/beam | [A] | 0.53 |
| Stored beam energy | [MJ] | 334 |
| Beam lifetime | [h] | 22 |
| Luminosity lifetime | [h] | 10 |
| Energy loss per turn | [keV] | 6.7 |
| Total radiated power per beam | [kW] | 3.6 |

Table 2.1: Overview of LHC performance parameters.

- CMS (Compact Muon Solenoid),

and four detectors designed for special tasks:

- ALICE (A Large Ion Collider Experiment),
- CASTOR (Centauro And STrange Object Research), searching for new effects in the very forward region in nucleus-nucleus collisions,
- LHCb, dedicated to CP violation studies in the $b$ quark sector,
- TOTEM (TOTal and Elastic Measurement), dedicated to the measurement of total cross section, elastic scattering and diffractive processes.

A schematic view of the collider ring with the various detectors is shown in Fig. 2.1. Both TOTEM and CASTOR will share the experimental cavern with CMS. They will also have a common trigger and data acquisition system.

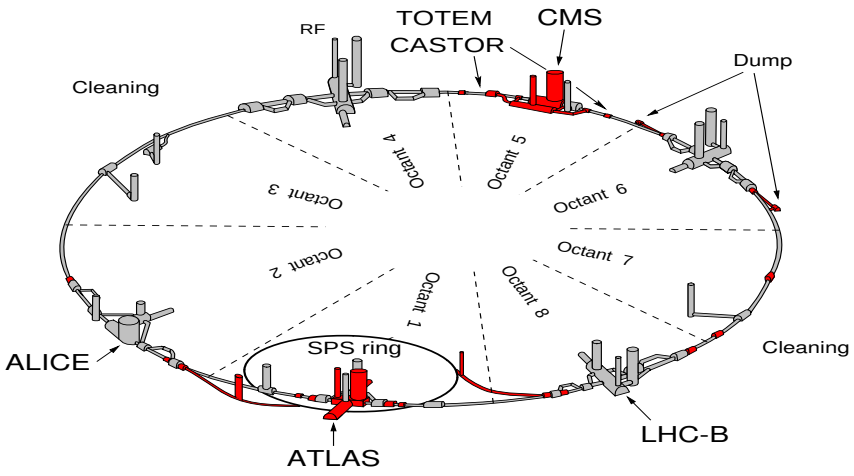


Figure 2.1: Overview of the LHC accelerator ring and the detectors

## 2.2 CMS Detector Overview

The overall layout of CMS is typical for a general purpose high energy particle detector (Fig. 2.2). It's designed in the form of a cylinder, with several layers of subdetectors, starting with a precise inner tracker, followed by electromagnetic and hadron calorimeters, and surrounded by the muon system. The original idea was to build a compact detector with very good muon measurement capabilities. The chosen configuration involves a superconducting solenoid capable of delivering a 4 T magnetic field, hence the name CMS - Compact Muon Solenoid.

The solenoid is 13 m long and has an inner diameter of 5.9 m. Such choice of dimensions has several advantages:

- The central tracker and both electromagnetic and hadron calorimeters can be located inside the solenoid, keeping the coil from affecting the calorimeter measurement.

- An iron yoke returning the magnetic flux can house the muon spectrometer, providing good resolution and acceptance for muons with rapidity up to 2.4, eliminating the need for extra forward toroids.

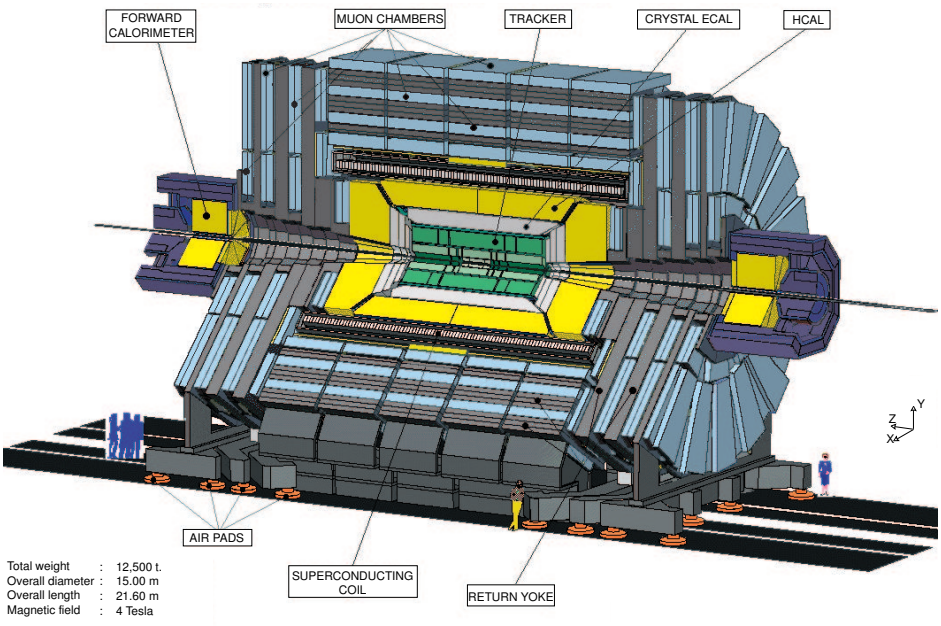


Figure 2.2: Overview of the Compact Muon Solenoid detector

The iron yoke provides mechanical support for the whole detector. It's divided into a barrel part, consisting of five wheels, and two endcaps consisting of 4 disks each. The central wheel supports the superconducting coil with the cryostat, housing the tracker as well as the barrel parts of the electromagnetic and hadron calorimeters. The endcap sections of the calorimeters are mounted on the iron disks and inserted into the solenoid from both ends. The whole structure has an outer diameter of 14.6 m and a length of 21.6 m. This is extended to 28.2 m by forward calorimeter modules mounted on the outer sides of the endcap disks.

## 2.3 The Muon System

### 2.3.1 Overview

The main goals of the muon system are: providing muon identification, trigger and momentum measurement, for muons with momenta from a few GeV to a few TeV. This can be achieved by constructing a spectrometer, with the muon

trajectory being bent by the 4 T magnetic field inside the solenoid and 1-2 T field in the outer muon system. Four stations of detectors are integrated into the iron return yoke. The muon trajectory is reconstructed from hits in these detectors combined with hits from the inner tracker.

Overall functionality and performance requirements imposed on the system by physics studies can be summarized as [24]:

- Muon identification: at least 16 $\lambda$ of material present up to $\eta = 2.4$ with no acceptance losses.
- Muon trigger: unambiguous beam crossing identification and trigger on single and multimuon events with well defined $p_t$ thresholds from a few GeV to 100 GeV and up to $\eta = 2.4$; provided by the combination of precise muon chambers and fast dedicated trigger detectors.
- Standalone momentum resolution from 8 to 15% $\delta p_t/p_t$ at 10 GeV and 20 to 40% at 1 TeV.
- Global momentum resolution after matching with the central tracker from 1.0 to 1.5% at 10 GeV, and from 6 to 17% at 1 TeV. Momentum-dependent spatial position matching at 1 TeV less than 1 mm in the bending plane and less than 10 mm in the non-bending plane.
- Charge assignment correct with 99% up to the kinematic limit of 7 TeV.
- Capability of withstanding the high radiation and interaction background expected at the LHC.

A schematic overview of the system is shown in Fig. 2.3. The muon detector is divided into three parts - the barrel, covering rapidity $|\eta|<1.3$ and two endcaps, covering the region $0.9<|\eta|<2.4$. Measurement of the muon trajectory is performed by Drift Tube detectors in the barrel and Cathode Strip Chambers in the endcaps. In addition to that, Resistive Plate Chambers are used throughout, providing fast, dedicated trigger and additional position measurement.

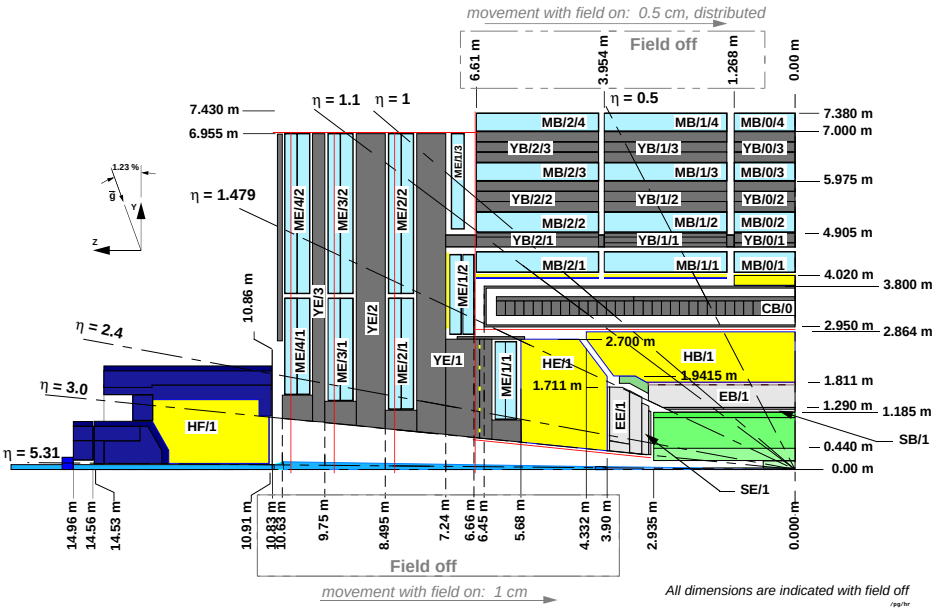


Figure 2.3: Longitudinal view of one quadrant of the CMS detector.

### 2.3.2 Drift Tubes (DT)

The choice of the drift tube as the main muon detector in the barrel, is motivated by the relatively low particle rates and magnetic field intensity in this region. The barrel section of the CMS iron yoke is divided into 5 wheels, forming 3 concentric layers of iron. Each wheel is divided into 12 sectors, as illustrated in Fig. 2.4. The muon chambers are installed on the outer and inner sides of the yoke and in the pockets between layers. In total there are 60 drift tube chambers in each of the three inner stations (MB1-MB3), and 70 in the fourth one (MB4).

The basic detector unit in this setup is a drift cell - a gas-filled tube with rectangular cross-section. The two shorter sides of the rectangle form cathodes, while an anode wire is strung through the middle. A charged particle passing through the detector volume ionizes the gas, producing a cloud of electrons, that drifts toward the wire. The drift time is measured and converted to distance using the knowledge of drift velocity.

The drift tubes in a chamber are grouped into *SuperLayers* (SL) consisting of four layers of tubes, staggered by half a tube. In each chamber there are

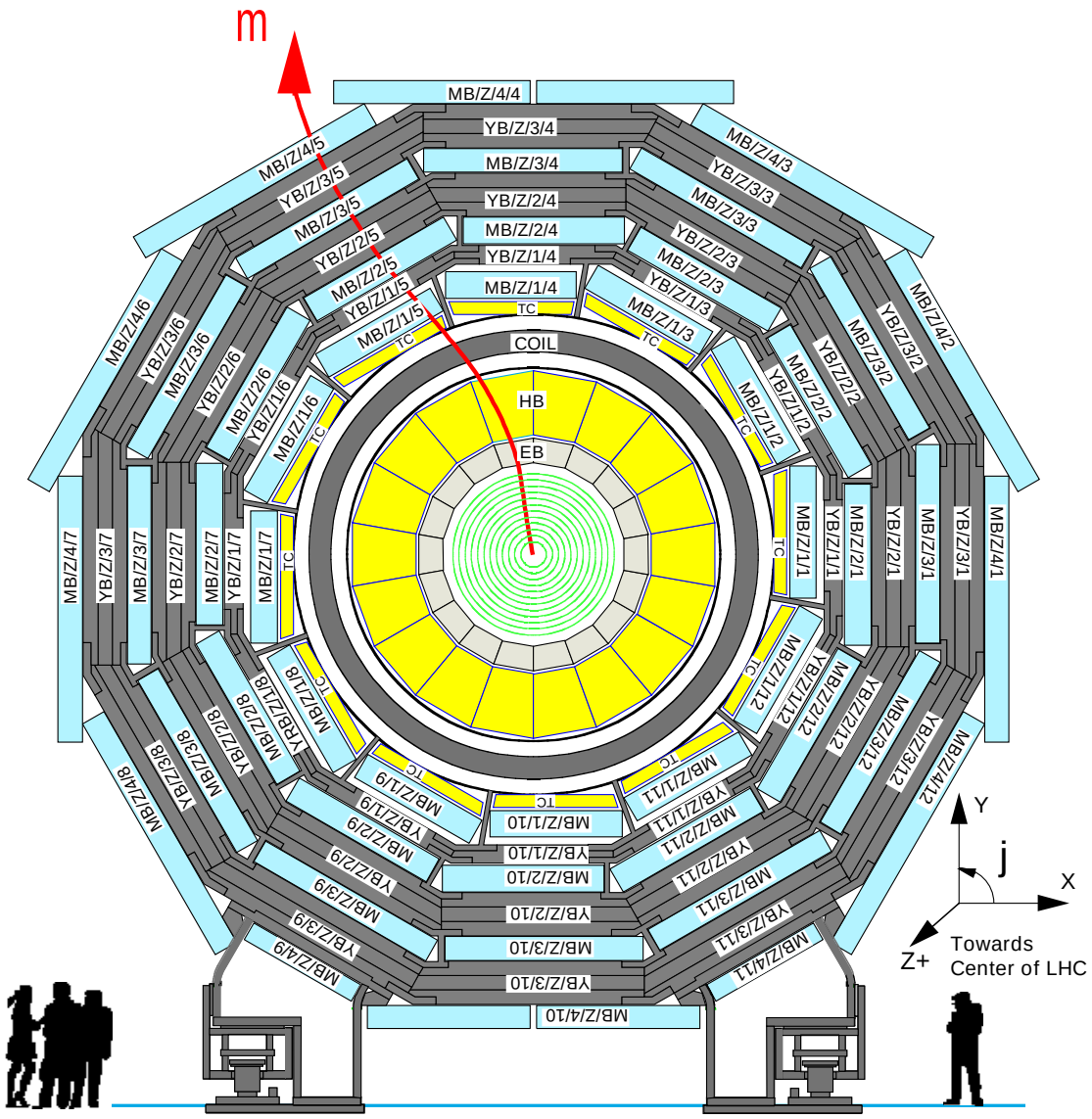


Figure 2.4: Transverse view of the CMS detector

two SLs with wires parallel to the beam direction, measuring muon position in the bending plane of the magnetic field. These are separated by a 128 mm thick aluminium honeycomb spacer, providing good angular resolution within one chamber. Additional SL measuring the $\eta$ coordinate of the muon is present in the three inner stations.

A single drift cell has a cross-section of $4 \times 1.1$ cm$^2$ and wire length between 2 m and 4 m. It is filled with a mixture of $Ar/CO_2$, giving a 350 ns maximum drift time. Single wire measurement resolution is of the order of 200 $\mu$m.

Each SL is equipped with fast pattern-recognition electronics, providing bunch crossing identification, and measuring the track segment position and angle with precision of 1.5 mm and 20 mrad, respectively. The precision of a single position measurement, after combining results from all SLs in a chamber, is of the order of 150 $\mu m$.

### 2.3.3 Cathode Strip Chambers (CSC)

Measurement of muon trajectory in the endcap part of the CMS muon system is performed mainly by Cathode Strip Chambers. This type of detector has been chosen because of it's capability to provide precise time and position measurement in the presence of a high and inhomogeneous magnetic field, and high particle rates.

The detector is a multiwire proportional chamber with one of the cathode planes being segmented in strips running orthogonally to the wires. The principle of operation is shown in Fig. 2.5: a muon crossing the chamber produces an avalanche in the gas (a mixture of Ar-$CO_2$-$CF_4$), running to the wire. This induces an electrical charge on the cathode strips. Fitting the measured distribution of charge picked up by the strips with the theoretical shape gives an estimate of the muon's position along the wire with precision up to 50 $\mu$m [25].

There are four muon stations integrated into each endcap of the CMS detector (ME1-ME4, see Fig. 2.3). The chambers are grouped into rings, with the first station (ME1) consisting of three rings, and the remaining three (ME2-ME4) having two rings of chambers. The chambers in every ring except the outermost

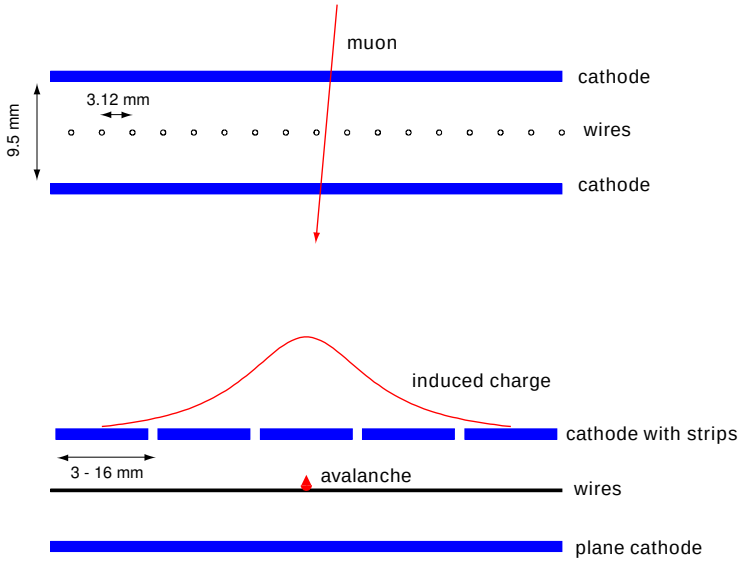


Figure 2.5: The principle of operation of a Cathode Strip Chamber, with cross-section across the wires (top) and across the strips (bottom).

ring of the first station (ME1/3) overlap in $\phi$, giving geometrical coverage close to 100%.

Each individual chamber has a trapezoidal shape, approximating a sector of a ring. Seven panels are stacked together, forming six gas gaps. Strip artwork is milled on one side of six of the panels, with the other side forming a continuous ground. The strips cover a constant area in $\phi$ (2.33-4.65 mrad, depending on the chamber) and have widths starting from 3.15 mm in the innermost chambers (ME1/1), to 16.0 mm in the outer CSC stations (ME2/2-ME4/2). The gap between strips is 0.5 mm (0.35 in ME1/1). Anode wires are wound onto both sides of even-number panels, spaced every 2.5, 3.12 or 3.16 mm. The wires are ganged into groups for readout, with widths from 16 mm to 51 mm.

### 2.3.4 Resistive Plate Chambers (RPC)

Resistive Plate Chambers are used throughout the CMS muon system, with the main goal of providing fast trigger signal.

A single chamber consists of two bakelite planes separated by a 2 mm wide gas gap. Electric field is generated with the help of two electrodes (high voltage

and ground), formed by covering the outer side of the planes with conductive graphite paint. Charged particles crossing the detector generate avalanches by ionizing the gas in the gap. The signal is read out from detector by a set of aluminium strips, insulated from the electrode with thin film.

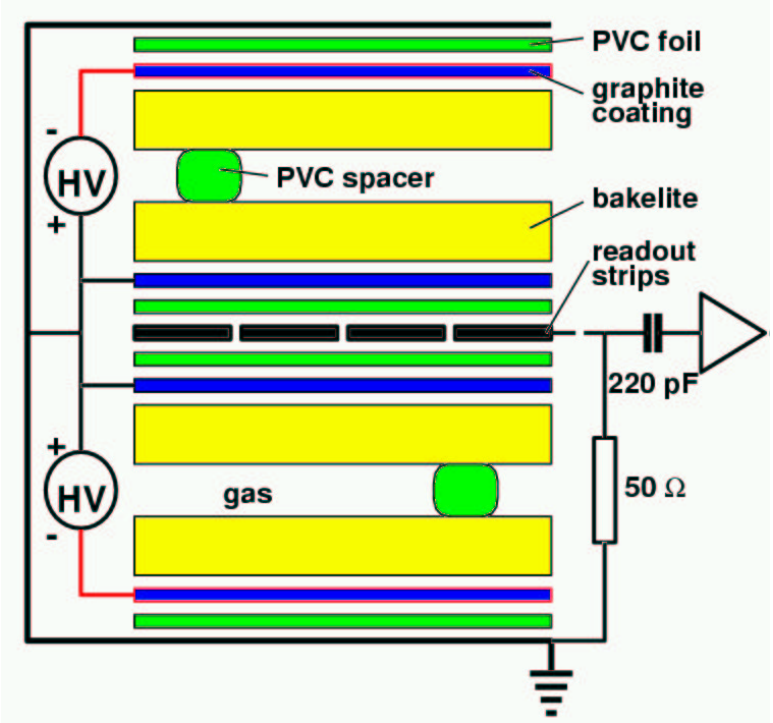


Figure 2.6: The double gap layout of CMS Resistive Plate Chambers

Efficiency of the detector can be improved by combining two gas gaps with a common readout plane (Fig. 2.6). This also allows for lower high voltage operation of individual gaps, increasing the rate capability.

The barrel RPC's are rectangular, with dimensions 210-375 cm $\times$ 85 cm. 96 readout strips run parallel to the beam, with widths increasing from the inner to the outer muon station, covering a constant angle of 5/16 degrees in $\phi$. There are six layers of RPC's in the CMS barrel muon system, two in the first and second muon station, and one in the third and fourth. In the endcaps, there are four stations, covering the region up to $\eta = 2.1$. Endcap RPC chambers are trapezoids, with strips running in the radial direction. The strips are also trapezoidal in shape, with a width changing to cover a constant 5/16 angle in $\phi$.

The strip length changes from about 25 cm to about 100 cm, depending on the $\eta$ region.

In order to achieve the fastest possible trigger response, muon candidate tracks are reconstructed from hits in the RPC chambers (at least three) by dedicated PAttern Comparator Trigger (PACT) electronics [26]. Predefined patterns corresponding to muons with different transverse momenta are compared with the actual detector response and a $p_t$ estimate is assigned to the track.

## 2.4 Inner Tracker

[27]

The central tracker system measures momentum of charged particles, such as electrons, muons and hadrons in jets. It's the innermost subdetector in CMS (closest to the interaction point), consisting of a silicon pixel vertex detector, surrounded by a silicon microstrip tracker.

There are 10 barrel layers and 9 endcap disks of single- and double-sided microstrip detectors. A single barrel module has dimensions of $64 \times 64\,\mathrm{mm}^2$, with a set of readout strips with 61-122 $\mu$m pitch. Two sided modules have a second set of strips on the other side, rotated by 100 mrad with respect to the interaction spot. Because of that, double sided modules are able to reconstruct the $z$ coordinate of the track. The precision of the measurement is 34 $\mu$m in $\phi$ and 320 $\mu$m in $z$. The total surface covered is $90\,\mathrm{m}^2$ in the barrel and $60\,\mathrm{m}^2$ in the endcaps, and the respective numbers of readout channels are $3.4 \times 10^6$ and $2.7 \times 10^6$.

The pixel detector consists of three barrel layers and two endcap disks of pixels. The layers are placed at radii of 41, 70 and 107 mm. The sensors and readout chips of the innermost layer are expected to survive the first four years of operation (assuming that this corresponds to two years of full luminosity running), and will be taken out when the LHC reaches it's design luminosity. The second layer should survive about 6-7 years, and after that time it will be replaced. The two disks extend for the radial range 60-150 mm and are placed 32.5 and 46.5 cm from the interaction point.

A single pixel is a square, covering an area of 150 $\mu$m $\times$ 150 $\mu$m. By interpolating the charge collected by neighboring pixels, a single hit resolution of 10-15 $\mu$m

can be achieved. The total surface area covered by the pixel sensors is $64\,\mathrm{m}^2$, and the total number of readout channels is $5.3 \times 10^6$.

Tracker resolution for single tracks can be parameterized as a function of the track momentum as $\frac{\Delta p_t}{p_t} = (15 \cdot \frac{p_t}{TeV} \oplus 0.5)\%$ in the barrel region ($|\eta| <= 1.6$) and decreases to $\frac{\Delta p_t}{p_t} = (60 \cdot \frac{p_t}{TeV} \oplus 0.5)\%$ in the tracker endcaps ($|\eta| = 2.5$). Single track efficiency is around 99%, for tracks forming jets it drops to 88%, with a ghost (fake) track rate of the order of 0.1%.

## 2.5 Calorimetry

The CMS calorimeter system is designed to measure the energy of hadronic jets and electromagnetic cascades induced by photons and electrons, and to provide hermetic coverage to allow missing transverse energy measurement. Other requirements are good electron and photon identification efficiency and good separation between QCD jets and hadronic $\tau$ decays. An overall energy resolution of the calorimeter system of $\frac{\sigma_E}{E} = \frac{100\%}{\sqrt{E}} \oplus 4.5\%$ is expected to be achieved.

### 2.5.1 Electromagnetic calorimeter (ECAL)

[28]

The CMS electromagnetic calorimeter is a scintillating crystal calorimeter, with lead-tungstate ($PbWO_4$) chosen as the crystal material.

The ECAL covers a region up to $|\eta| = 3$, with the barrel part extending from $\eta = 0$ to $|\eta| = 1.5$ and the endcap covering $1.5 < |\eta| < 3$. A schematic view of the calorimeter design is shown in Fig.2.7. An additional preshower detector will be installed in front of the endcap, covering $1.65 < |\eta| < 2.61$. This detector consists of to lead converters and planes of silicon strips, and it's main function will be providing additional information to distinguish $\pi^0$'s from photons. An option of adding a barrel preshower in $|\eta| < 0.9$ for high luminosity operation is also being considered.

The granularity of the calorimeter is $\Delta\eta \times \Delta\phi = 0.0175 \times 0.0175$ in the barrel and up to $\Delta\eta \times \Delta\phi = 0.05 \times 0.05$ in the endcaps. The barrel crystals have dimensions $22 \times 22 \times 230$mm, this changes to $25 \times 25 \times 220$mm for the endcaps.

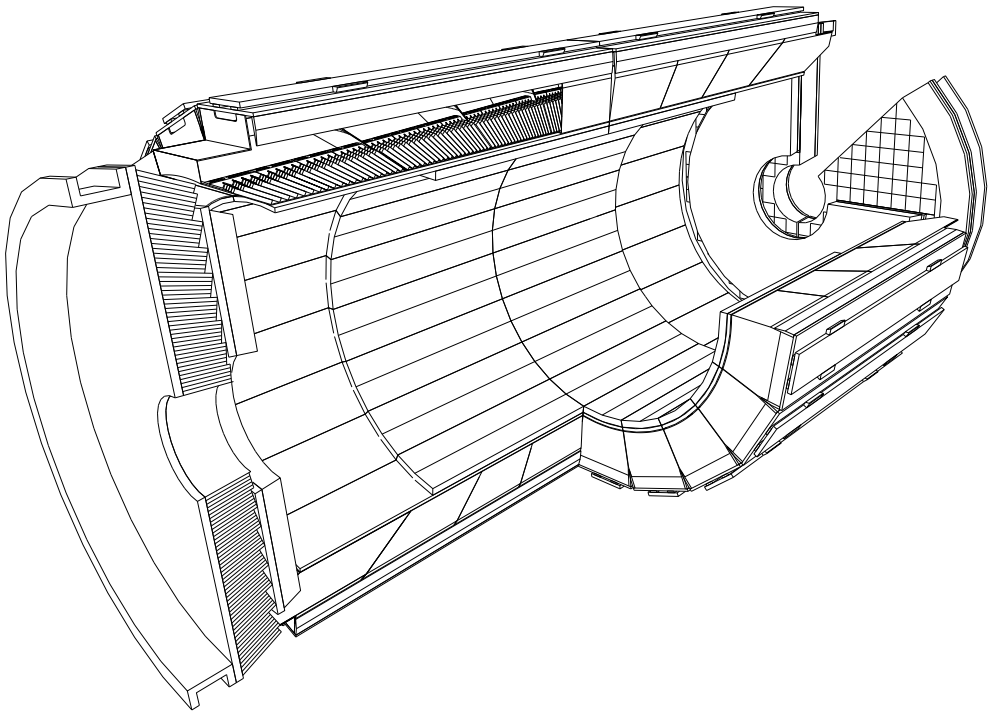

Figure 2.7: The CMS electromagnetic calorimeter

The choice of transverse dimensions is motivated by the $PbWO_4$ Molière radius of 21.9 mm. The depth of the crystals corresponds to 26 $X_0$ radiation lengths.

The resolution for single photons with energies of 25-500 GeV can be parameterized as $\frac{\sigma_E}{E} = \frac{2.7\%}{\sqrt{E}} \oplus \frac{155\,MeV}{E} \oplus 0.55\%$ for the barrel part and $\frac{\sigma_E}{E} = \frac{5.7\%}{\sqrt{E}} \oplus \frac{205\,MeV}{E} \oplus 0.55\%$ for the endcap. These numbers are given for low luminosity running ($10^{33} cm^{-2} s^{-1}$), for high luminosity the noise (the middle term in the equation) rises to 210 MeV and 245 MeV for the barrel and endcap, respectively.

### 2.5.2 Hadronic calorimeter (HCAL)

[29]

The hadronic calorimetry system in CMS consists of three subdetectors: the Central Hadron Calorimeter (divided into the barrel (HB) and endcap (HE) part), the Outer Hadronic calorimeter (HO) and the Forward calorimeter (HF).

The central calorimeter is a sampling calorimeter located inside the magnetic

coil, consisting of plastic scintillator tiles inserted between copper absorber plates. The copper is 5cm thick in the barrel and 8cm thick in the endcaps, and the scintillator tiles are 4 mm thick. The choice of copper for the absorber material was motivated by the fact that the detector is located inside the CMS solenoid, and a non-magnetic material that doesn't distort the magnetic field was necessary. Signal is read out by wavelength-shifting plastic fibers and transformed into electrical pulses by hybrid photo diodes. The segmentation of the barrel calorimeter is $\Delta\eta \times \Delta\phi = 0.087 \times 0.087$, and the depth is about 79 cm, corresponding to $5.15\,\lambda$.

Small radiation depth in the barrel justifies the need for the outer calorimeter, which is placed outside the superconducting coil, together with the first muon station. Two additional sampling layers are placed there (three in the central wheel) to ensure full containment of the hadronic showers.

Hermecity of the hadron calorimeter is extended to $|\eta| < 5$ by adding the forward calorimeter, located outside of the muon endcaps, 11 m from the interaction point. The detector is a large copper block with embedded quartz fibers. The fibers run parallel to the beam and pick up Cherenkov light from particles forming showers in the copper absorber. The active part of the forward calorimeter has a radius of 1.4 m, with a 25 cm hole in the middle for the beam pipe. The depth of the detector is 1.65 m, ensuring the containment of Cherenkov light produced by hadrons up to 1 TeV. Lateral segmentation is achieved by using fibers of three different lengths - 165 cm, 143 cm and 30 cm.

According to the Technical Proposal, the CMS hadron calorimeter resolution will range from $\frac{\sigma_E}{E} = \frac{65\%}{\sqrt{E}} \oplus 5\%$ in the barrel part (at $\eta = 0$) and $\frac{\sigma_E}{E} = \frac{83\%}{\sqrt{E}} \oplus 5\%$ in the endcaps, to $\frac{\sigma_E}{E} = \frac{100\%}{\sqrt{E}} \oplus 5\%$ in the forward calorimeter.

## 2.6 Summary of detector performance

The overall performance of the CMS detector is briefly summarized in Table 2.2.

| | |
|---|---|
| Tracker momentum resolution for single particles | $\frac{\Delta p_t}{p_t} = ((15-60)\cdot\frac{p_t}{TeV}\oplus 0.5)\%$ |
| ECAL single photon energy resolution | $\frac{\sigma_E}{E} = \frac{(2.7-5.7)\%}{\sqrt{E}}\oplus\frac{(155-205)\,MeV}{E}\oplus 0.55\%$ |
| HCAL single particle energy resolution | $\frac{\sigma_E}{E} = \frac{(65-100)\%}{\sqrt{E}}\oplus 5\%$ |
| Single muon momentum resolution for muon energies 0.05-2 TeV | $\frac{\Delta p_t}{p_t} = 4\%\cdot\sqrt{p_t/TeV}$ |

Table 2.2: CMS detector performance overview

## 2.7 The Trigger

[30], [31]

Fig. 2.8 shows the rates of different processes expected in CMS during high luminosity runs. In the LHC collider, proton bunch crossings will occur ever 25 ns, giving a 40 MHz event rate. The goal of the CMS trigger system is to reduce this by many orders of magnitude, down to a mere 100 Hz. This target rate is still large, if one takes into account the fact that the size of a single event is expected to be around 1 MB, and the data will still need to be saved with a 100 MB/s rate. This corresponds to about 80 DVD-R discs filled in an hour.

Performing the reduction of event rate to the chosen level is the task of the Trigger. In CMS, a two-step trigger has been developed. The Level-1 (L1) trigger is based on custom electronics, and performs initial rate reduction with a target output to 100 kHz. The time for decision is 3.2 $\mu$s. The High Level Trigger system (HLT) is realized with software running on a farm of commercially available processors, and brings the rate down to 100 Hz.

Event selection in the L1 trigger is based on information about muons, electrons, photons, jets and missing transverse energy. Physics requirements for leptons are: efficiency larger than 95% in the $|\eta| < 2.5$ region with a $p_t > 40$ GeV threshold for single leptons and $p_t > 20$ and 15 GeV for dileptons. Similar performance is required for photon and diphoton triggers. Jet and multi-jet triggers

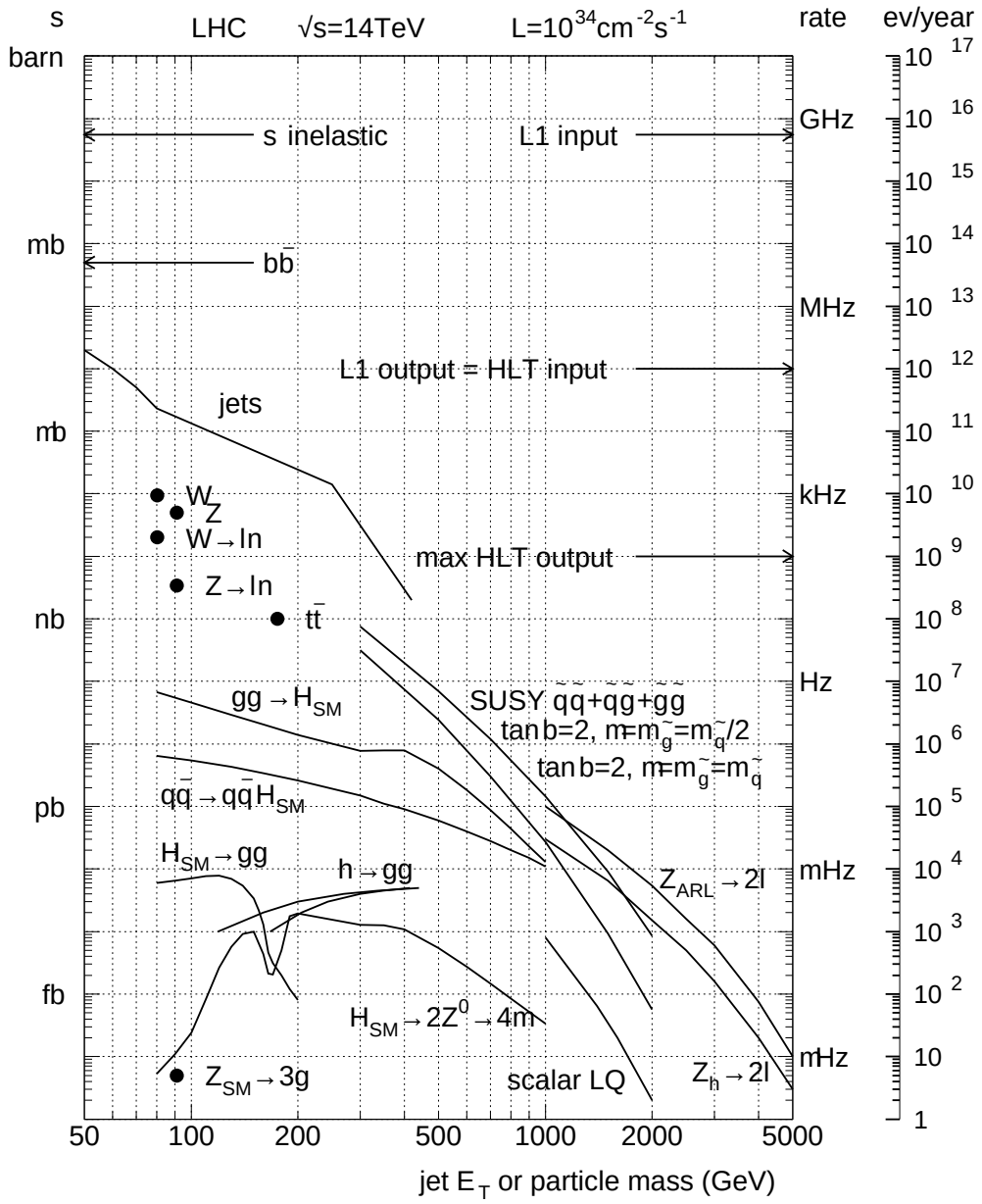


Figure 2.8: Event rates and cross sections of selected processes for the LHC design luminosity of $10^{34} cm^{-2} s^{-1}$.[30]

should have a well defined efficiency in the whole $|\eta| < 5$ region in order to provide results overlapping with lower energy data from other colliders. The missing energy trigger is required with a 100 GeV threshold.

The L1 trigger is structured as follows: the information from the ECAL and both central and forward hadronic calorimeters is processed by the Regional Calorimeter Trigger, where electron, photon, tau and jet candidates are looked for. Those candidates are transmitted to the Global Calorimeter Trigger (GCT), which sorts them and forwards the 4 most energetic ones to the Global Trigger. In addition to that, the GCT provides an $(\eta, \phi)$ map of quiet regions and calculates global quantities, like the total transverse energy and total missing energy vector. The three muon subsystems (DT, CSC and RPC) send information to the Global Muon Trigger (GMT), where an attempt to correlate the candidate DT and CSC tracks with RPC tracks is made. Muon isolation is checked using the quiet tower data from the GCT. The muons are sorted according to their quality, correlation and $p_t$ and the top four candidates are sent to the Global Trigger.

The Global Trigger accepts and synchronizes muon and calorimeter trigger information and produces the L1 Trigger decision based on the data. If a bunch crossing is accepted, a Level-1 Accept signal is sent to the Timing Trigger and Control system (TTC), which in turn notifies the detector sub-systems to initiate readout.

The final stage of the CMS trigger is the fully programmable HLT running on a single farm of an estimated number of 2000 CPU's. In order to reject events as fast as possible, reconstruction in the HLT is done in several stages, starting from simple local reconstruction, followed by incorporating information from different subdetectors in more complex algorithms.

# Chapter 3

# Signal generation, detector simulation and reconstruction

Particle interactions in proton-proton collisions were simulated with PYTHIA 6.224 [15] Monte-Carlo generator. The hard scattering process was generated via a leading order matrix element calculation, followed by a parton shower evolution of the resulting partons and fragmentation, forming the final state particles. The CTEQ5L [32] structure function set was used.

The output from the generator was processed through detailed detector simulation and reconstruction software to approximate a realistic experimental situation. Particle tracking and detector response was simulated by OSCAR (Object oriented Simulation for Cms Analysis and Reconstruction) [33], a CMS detector simulation program based on the GEANT4 [34] package. The result is a collection of simulated hits (SimHits) in the sensitive elements of the detector - particle entry/exit points, energy losses, etc.

The last two steps, digitization and reconstruction, were performed by ORCA (Object oriented Reconstruction for Cms Analysis) [35]. The digitization step consists of simulating the response of detector readout and data acquisition systems, with the output intended to resemble the output of a real working detector. The final step is the reconstruction of physical objects (particle tracks, jets, missing energy) and the simulation of the Level-1 and High Level Triggers. A combination of single and double muon triggers was used in this analysis, with the requirement of muon isolation removed. The Level-1 thresholds were 3 GeV for two muons and 14 GeV for single muons. The HLT required two muons with

momentum above 11 GeV or one muon with momentum above 26 GeV. The combined L1+HLT trigger efficiency for the signal and background data samples was between 95 and 97%.

## 3.1 Monte-Carlo sample generation

### 3.1.1 Signal

The signal process has been selected in PYTHIA by switching on two subprocesses $MSUB(392)$ and $MSUB(391)$, corresponding to the two graviton production processes in proton-proton interaction (quark-quark annihilation and gluon fusion). Only the muon decay channel of the graviton has been left open, and an $|\eta| < 2.5$ kinematic cut was imposed on the decay products with the $CKIN(13)$ - $CKIN(16)$ switches. An additional 10 GeV cut on the $p_t$ of all particles was applied for every event.

A total number of 19 signal samples of 5000 events each were generated for different values of the graviton mass (from 1 TeV to 4 TeV) and coupling (from 0.01 to 0.2). The simulated points were chosen to cover the $5\sigma$ reach region established previously with fast simulation [16]. Cross-sections for the generated samples are shown in Table 3.1.

### 3.1.2 Background

Drell-Yan background has been generated by selecting the $MSEL = 11$ process. A 10 GeV $p_t$ cut was imposed on all particles, and only events with two muons in the final state were saved. In order to provide the necessary statistics in a broad range of dimuon invariant masses, the background was generated in several $\hat{p_t}$ bins, with 10000 events in each bin. The dimuon invariant mass spectrum is shown in Fig. 3.1. Cross-sections of the generated background samples are shown in Table. 3.2. Also shown are the preselection efficiencies, calculated as the ratio of events containing two $p_t > 10$ GeV muons to all the generated events. The cross-sections were multiplied by a constant K-factor equal to 1.30 to take into account higher order corrections [36].

| Sample | Graviton mass [GeV] | $k/M_{Pl}$ | Cross-section [fb] |
|---|---|---|---|
| g10c01 | 1000 | 0.01 | 5.843 |
| g10c02 | 1000 | 0.02 | 23.68 |
| g15c01 | 1500 | 0.01 | 0.722 |
| g15c02 | 1500 | 0.02 | 2.828 |
| g15c05 | 1500 | 0.05 | 17.55 |
| g20c01 | 2000 | 0.01 | 0.1344 |
| g20c02 | 2000 | 0.02 | 0.5353 |
| g20c05 | 2000 | 0.05 | 3.314 |
| g25c02 | 2500 | 0.02 | 0.1341 |
| g25c05 | 2500 | 0.05 | 0.8241 |
| g25c10 | 2500 | 0.10 | 3.354 |
| g30c02 | 3000 | 0.02 | 0.0387 |
| g30c05 | 3000 | 0.05 | 0.2405 |
| g30c10 | 3000 | 0.10 | 0.9615 |
| g35c05 | 3500 | 0.05 | 0.0749 |
| g35c10 | 3500 | 0.10 | 0.3026 |
| g35c20 | 3500 | 0.20 | 1.170 |
| g40c10 | 4000 | 0.10 | 0.1030 |
| g40c20 | 4000 | 0.20 | 0.4014 |

Table 3.1: Cross-sections of generated signal samples.

$Z'$ production was also simulated, for use in the analysis of $Z'$-graviton discrimination. The $Z'$ masses corresponded to masses of the generated gravitons. A total of 7 data samples was produced, with 5000 events each. The production cross-sections were ignored, the $Z'$ samples were normalized to give the same numbers of signal events as the gravitons they were tested against.

| Sample | $\hat{p_t}$ range [GeV] | Cross-section [fb] | Preselection efficiency |
|---|---|---|---|
| drellm01h05 | 100-500 | $4.854\times10^{7}$ | 3.38% |
| drellm05h10 | 500-1000 | 1644 | 6.14% |
| drellm10h15 | 1000-1500 | 97.80 | 6.26% |
| drellm15h20 | 1500-2000 | 14.35 | 6.42% |
| drellm20h25 | 2000-2500 | 3.055 | 6.31% |
| drellm25h35 | 2500-3500 | 1.022 | 6.37% |
| drellm35h45 | 3500-4500 | $9.517\times10^{-2}$ | 6.52% |

Table 3.2: Cross-sections and preselection efficiencies for generated background samples.

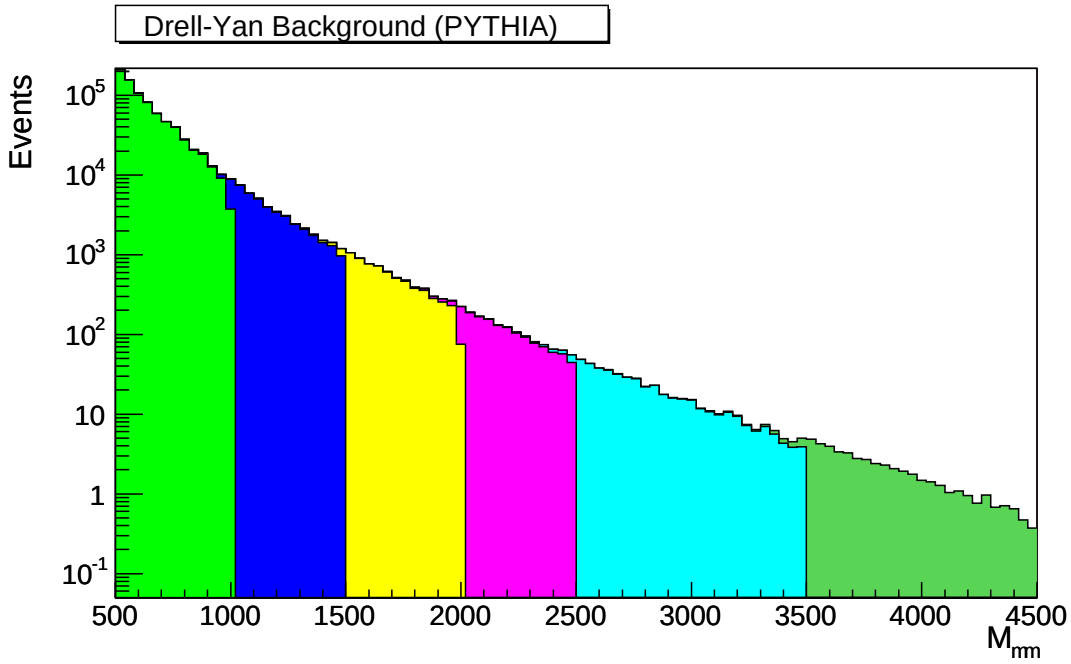


Figure 3.1: Invariant mass spectrum of the simulated Drell-Yan background. Different colors correspond to different $\hat{p_t}$ bins.

## 3.2 Muon reconstruction in CMS

In CMS, the information about muon momentum comes from two detector subsystems - the inner Tracker and the Muon System. The measurement is performed by reconstructing the muon trajectory and determining it's momentum from the track's curvature in the magnetic field. The components of the momentum measurement procedure are:

- Local muon reconstruction - the first stage of reconstruction in the Muon System, performed at the level of individual muon chambers.
- Regional muon reconstruction - the step where information from different muon stations is combined to reconstruct tracks in the muon system.
- Global muon reconstruction - the last step in muon reconstruction, combining the information from the tracker and the muon system into the final momentum measurement.

These are described in detail in the following sections.

### 3.2.1 Local reconstruction in the muon detectors

#### 3.2.1.1 Drift Tubes

The task of the Drift Tube (DT) regional reconstruction algorithm is to reconstruct track segments in individual muon stations based on the information from the 12 (or 8 in case of the last muon station) layers of drift cells.

The first step is the reconstruction of muon hit positions in the cells themselves. The input information from the detector is a TDC measurement, which is converted to drift time after synchronization, taking into account electronics delays, signal propagation along the wire and the time-of-flight of the muon from the vertex. Each measurement corresponds to a pair of hits, located on both sides of the wire. This so-called left-right ambiguity is solved during segment reconstruction. The hit position[1] is calculated as a function of the drift time, the track incidence angle (the angle between the track and the normal direction to

[1]Namely the distance between the muon track and the cell wire in the layer plane.

the chamber), and the components of the cell magnetic field parallel and perpendicular to the wire in the radial direction. Since the position of the hit along the wire is not known at this point, average values are assumed for the signal propagation time along the wire and the cell magnetic field. Also, the track incidence angle in not yet determined. As this information becomes available during segment reconstruction, the hit measurement is subsequently refined. The segment reconstruction procedure proceeds in three steps:

- segment candidate building,
- ambiguity resolution between candidates sharing hits,
- combining segments in the $r$-$\phi$ and $r$-$z$ projections.

A schematic view of a drift chamber with the different elements of segment reconstruction is shown in Fig. 3.2. The first two reconstruction steps are performed independently in the $r$-$z$ and $r$-$\phi$ superlayers (for the $r$-$\phi$ projection both superlayers are used together). Segment building starts by looking in the first and last layer for pairs of hits compatible with a track originating from the nominal beam spot. For each pair, hits compatible with the segment are searched for in the remaining layers. If more than one hit is found in a layer, the number of segment candidates is increased to take all hits into account. After all layers have been considered, the segment with the largest number of hits and smallest $\chi^2$ is kept. The procedure is then repeated for remaining starting hit pairs.

In the second step, ambiguities are resolved by taking any two segments sharing one or more hits and discarding the one with a smaller number of hits or a larger $\chi^2$. For each segment, the cell hits are updated using the segment incidence angle, and the segment is refitted with the new hits. The third step combines all the reconstructed segments in the two projections, forming 4-dimensional segments in space (2-dimensional starting point and 2-dimensional direction). Since the position of individual hits along the wire is now known, the hit positions can be updated with the new information, and the segments are again refitted with the new hits. This step is not performed for the fourth muon station, as the $r$-$z$ superlayer is not present there.

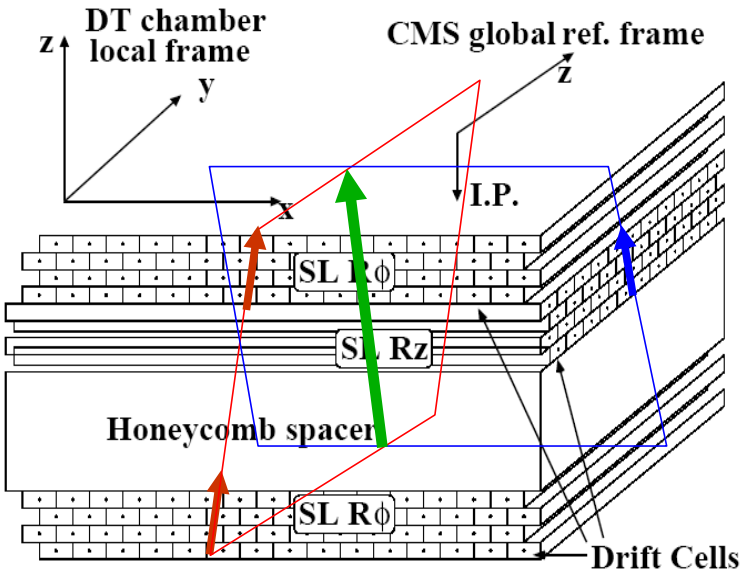


Figure 3.2: RecHits in a Drift Tube chamber. The 2D reconstructed segments in the Super-Layers are shown in red and blue, and the 4D RecHit combined from the two is shown as the green arrow.

#### 3.2.1.2 Cathode Strip Chambers

The output of the Cathode Strip Chamber (CSC) regional reconstruction algorithm is a set of 4-dimensional track segments, similar to the ones produced by the DT system. The input is the signal from the strips, measured by a switched capacitor array (SCA) and the set of wire groups that gave a signal.

The strip signal reconstruction starts with determining the pulse heights from SCA data. This is done by selecting the largest of the available 8 samples (sampled every 50ns) and subtracting from it's height the average height of the first two time samples to provide a correction for baseline shifts. The expected error from calibration uncertainty (3%) and noise ($\sim$ 1.5%) is also taken into account. The hit position is then reconstructed by fitting a "Gatti" distribution [37] to the pulse heights on three adjacent strips. Two dimensional hits are then formed for every layer by taking the combinations of all the strip hits with all the fired groups of strips occurring withing two bunch crossings of each other.

The next step is the segment reconstruction. The starting points for a segment are two most separated hits in the layers 1 and 6, with a requirement that their $r$-

$\phi$ separation in not larger than 1 cm. The intermediate layers are then considered one at a time by searching for hits within 2.5 mm in $r$-$\phi$ from the segment and updating the line fit if a hit was found. If more than one compatible hit is found in a layer, the one giving the best $\chi^2$ is used. The segment is kept if the total number of hits is at least 4. Then the hits are flagged as used and the procedure is repeated starting from another pair of unused hits in the chamber.

#### 3.2.1.3 Resistive Plate Chambers

Since the Resistive Plate Chambers (RPC) consist of just a single detector layer, the result of local reconstruction is just a point in the chamber plane. The reconstruction algorithm proceeds by grouping adjacent fired strips into clusters, and the result is the center-of-gravity of each cluster. The average cluster size is of the order of 1.5 strips. The position errors are computed assuming that the charged particle that produced the signal could cross the detector in any point in the area covered by the clustered strips, with flat probability. This assumption is intended as a compromise between the fact that the muon is most likely to have crossed the detector in the center of the cluster, and the effect of secondary particles accompanying the muon, which can extend the cluster from the muon in one or the other direction. The $x$ and $y$ errors are different since the RPC strips have lengths of the order of 1 m and widths of the order of centimeters.

### 3.2.2 Standalone muon reconstruction

After muon track segments have been found in the muon stations, the trajectory of the muon in the muon system can be reconstructed. The starting element for trajectory reconstruction is the seed - a coarse estimate of the particle's position, momentum and direction, derived from the track segment reconstructed at the second muon station. This state is extrapolated to the first muon station, where trajectory building starts. The GEANE [38] package is used to simulate muon propagation in inhomogeneous magnetic field, taking into account energy loss in the material and multiple scattering.

The trajectory is built using a Kalman filter technique [39]. In the first step, a measurement compatible with the trajectory is searched for in the first muon

station, and if found, the track parameters and errors are updated. The trajectory is then propagated to the next station and the procedure is repeated. After reaching the outer station, another Kalman filter is run in the opposite direction, resulting in a track estimate at the innermost station. This is further improved by performing an additional fit with the assumption that the muon originated from the nominal beam spot region ($\sigma_{xy} = 15\mu$m and $\sigma_z = 5.3$ cm).

The hits used in this fit have different structure in the various muon subdetector systems - 2D segments are used in the drift tubes, while in the endcaps individual points from the CSC layers are used, because of the highly inhomogeneous magnetic field. The RPC hits are also used in trajectory building, supplementing the information from the more precise DT and CSC measurement especially in the barrel-endcap overlap region.

Currently two versions of this algorithm are used in ORCA, with a different choice of seeds. L2MuonReconstructor is seeded by the Level-1 trigger, while StandAloneMuonReconstructor generates seeds internally, from the reconstructed hits in the muon system. Both share the same trajectory-building algorithm.

### 3.2.3 Global Muon reconstruction

In the final step of muon reconstruction, information from the tracker is added to the track fit. Again, two versions of the algorithm, with different seeds, are available. L3MuonReconstructor is seeded by L2MuonReconstructor, and GlobalMuonReconstructor is seeded by StandAloneMuonReconstructor. The seed in this case is the output of the regional reconstruction algorithm, namely the trajectory parameters and errors at the innermost muon station. The reconstruction procedure consists of the following elements:

- defining a "region of interest" in the tracker,
- reconstructing tracker trajectories in the chosen region,
- adding hits from the muon system to the reconstructed trajectories.

First, the seeds from the muon system are used to define a region in the tracker where, in the next step, the muon trajectory is searched for. This is a crucial

point, since the size of the region determines the efficiency, fake rate and CPU time used for reconstruction. The size is chosen based on the trajectory seed parameter errors, so for better quality muons reconstructed in the muon system the region can be smaller.

The second step is the reconstruction of trajectories in the tracker. It starts from the generation of seeds in the selected region. Every hit pair coming from two different tracker layers (pixel or double-sided silicon strip layer) is considered. For every such pair the track is propagated from the beam spot to the inner and outer hits, to obtain the initial trajectory parameters. Then, each seed is used to grow a trajectory. Trajectory growing starts by generating all possible trajectories with a Kalman filter algorithm. The track parameters are propagated layer by layer from the innermost pixel to the outermost silicon layers, and at each layer the measurement is updated with information from hits compatible with the trajectory. If there's more than one hit found, the number of trajectories is increased to take each one into account. When the edge of the tracker is reached, a "trajectory cleaning" algorithm is applied, where ambiguities between trajectories built from the same seed are resolved, based on the $\chi^2$ of the fit and the number of hits in a trajectory.

The third step consists of fitting the resulting trajectories with the beam spot constraint removed, and with the hits from the muon system included. The resulting tracks are cleaned again, and a final "trajectory smoothing" is applied - a combination of forward and backward Kalman filters, resulting in an optimal estimate of trajectory parameters at every measurement layer.

## 3.3 Custom offline improvements in muon reconstruction

In order to improve reconstruction of very energetic muons, some additions to the default code were made. Some of them are now (since January 2006) part of the official CMS muon reconstruction algorithm [40]. The performance of the muon system is shown in Figs. 3.3 and 3.4.

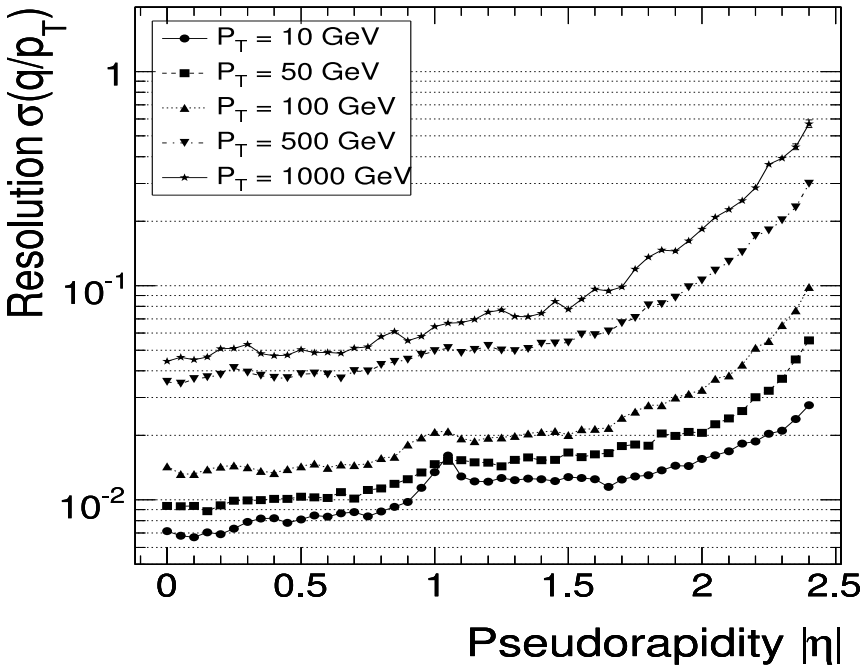


Figure 3.3: CMS muon transverse momentum resolution for different values of muon momentum and pseudorapidity [40].

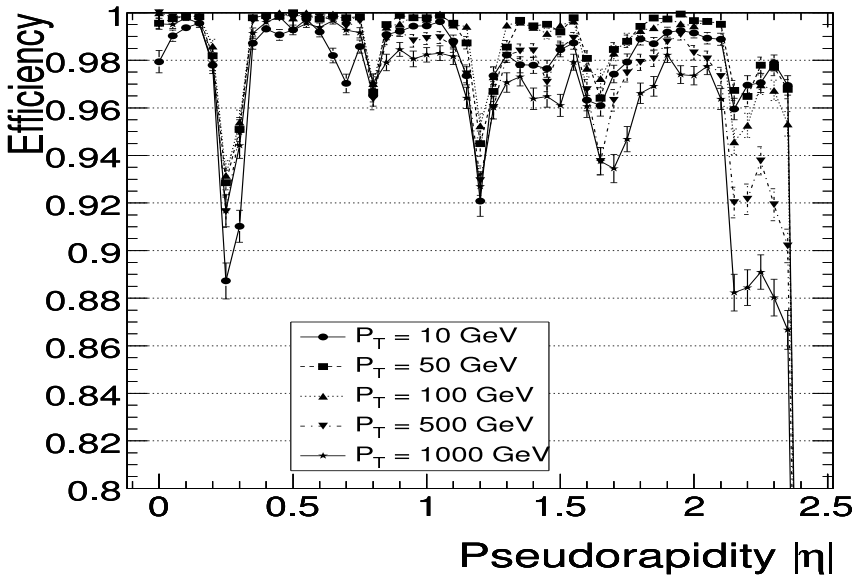


Figure 3.4: Efficiency of the CMS muon system for different values of muon momentum and pseudorapidity [40].

### 3.3.1 The Picky Muon Reconstructor

Momentum measurement precision in a muon spectrometer is limited by several factors. These can be divided into two categories. The first one is stochastic physics processes - multiple scattering, energy loss and electromagnetic showering. The second category is detector-related effects - measurement precision, magnetic field uncertainty and detector misalignment. Here, we will focus on electromagnetic showers, as it's the main source of physical uncertainty for muons with energies in the TeV range - for muon momenta below 100 GeV multiple scattering becomes dominant.

There are four main processes describing muon energy loss in material:

- ionization, including production of delta rays (knock-on electrons with energies from single eV to ∼100 GeV),
- direct electron-positron pair production,
- bremsstrahlung,
- inelastic interaction with nuclei.

Figure 3.5 shows the probabilities for emitting electrons of different energies by muons propagating through iron. As can be seen from the plot, the cross-sections for electron production rise with muon momentum, especially the cross section for pair production. For a muon with 1 TeV energy, this process dominates for highly energetic (above 1 GeV) electrons. Electrons above 1 GeV are the source of electromagnetic showers that contaminate muon detectors. A thousand TeV muons traversing 1 meter of iron will produce an average of sixty 1 GeV electrons through ionization, two through bremsstrahlung and 500 through pair production.

In the CMS outer muon system the possibility of showering is taken into account by placing the four muon stations between layers of iron from the CMS solenoid return yoke. The thickness of the iron (30 cm to 90 cm) is sufficient to contain most of the electromagnetic showers caused by muons [42]. This way, even if a shower in one muon station corrupts the position measurement in that station, it shouldn't affect the next stations (except for cases where the muon lost a significant fraction of it's energy and it's direction has changed). So in

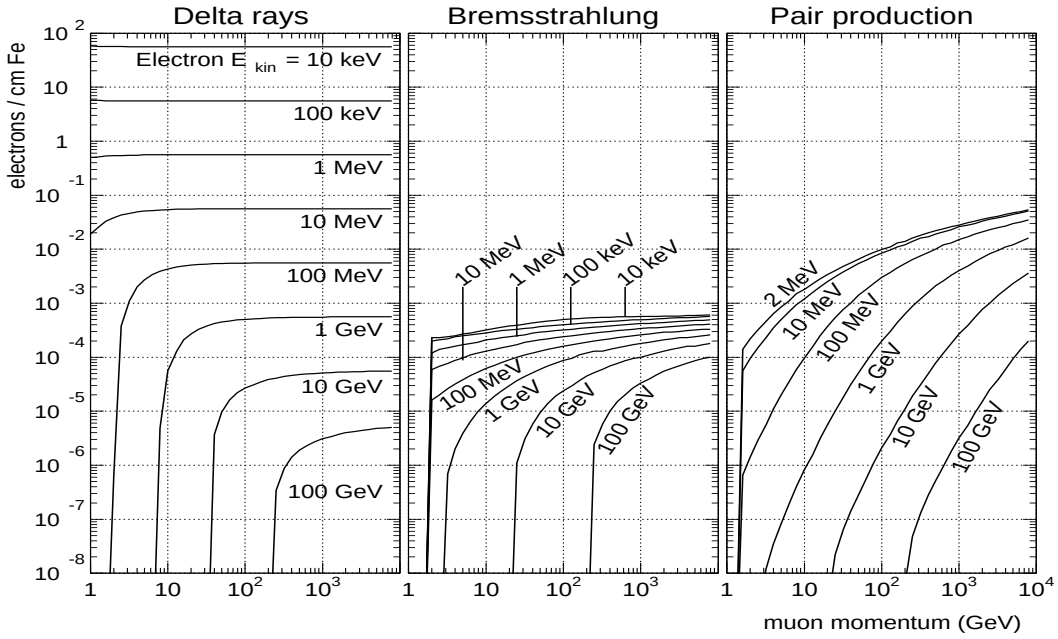


Figure 3.5: Cross sections for electron production by muons traversing matter. Shown as number of electrons produced per 1 cm of iron. Plot taken from [41]

principle, the station where the shower occurred should be simply removed from the track fit.

Analyzing the reconstruction of simulated energetic single muon events yields a few observations:

- The reconstruction algorithm selects the reconstructed segment that best matches the muon track. In most cases, even when there's a shower, the correct muon track can still be found among all the other tracks and the reconstructor usually manages to do that.
- Sometimes the muon track is not visible or it's incorrectly reconstructed - for example in the drift tubes, if an electron crosses the same drift tube as the muon, but closer to the wire, the muon hit is lost and the electron hit is used in reconstruction instead.
- Such corrupt measurements can significantly alter the overall muon momentum estimation.

- Discarding all hits in the stations following the one with the shower usually gives worse results than discarding just the contaminated station.

A procedure has been set up to identify the stations containing showers and removing them from the fit, but only in the case when the measurement differs significantly from the muon track. It was implemented as a modification of the standard GlobalMuonReconstructor (GMR) ORCA class. The algorithm works as follows: first, the default global reconstruction is performed, but during the final step where muon hits are added to the fit, for every hit considered, the multiplicity of hits in the chamber that produced it is checked. This is done in a cone with predefined radius around the hit being used in trajectory building, to ignore random hits eg. from neutron background. If the number of hits in the chamber is higher than one, the chamber is flagged as contaminated. After the fit is complete, the compatibility of the hits in contaminated chambers with the trajectory is checked by performing a $\chi^2$ cut. Also, an additional loose $\chi^2$ cut is applied to all hits in the tracker and the muon system. Then, the fitting and smoothing procedure is applied to the set of hits that passed the cuts. The class performing reconstruction with the modified algorithm has been called the PickyMuonReconstructor (PMR).

The parameters of the algorithm ($\chi^2$ and hit number cut values) were optimized on samples of 9000 single muons with energy of 1.5 TeV separately for the barrel and the endcaps of the muon system. The results are shown in Fig. 3.6. The PMR is mainly sensitive to significant errors in reconstruction, where a wrong hit has been taken into account, so the main improvement is in the non-gaussian tails of the resolution function. This results in a significantly lower RMS of the distribution for the new algorithm. Another quantity used during optimization, besides RMS, is "effective efficiency" - defined as the fraction of muons with reconstructed momentum within 20% of the true value. Performance characteristics of the two reconstructors are summarized in Table. 3.3.

A sample of 7000 low energy (50 GeV) muons was also used to check that the reconstruction performance does not degrade for muons with low momentum (Fig. 3.7).

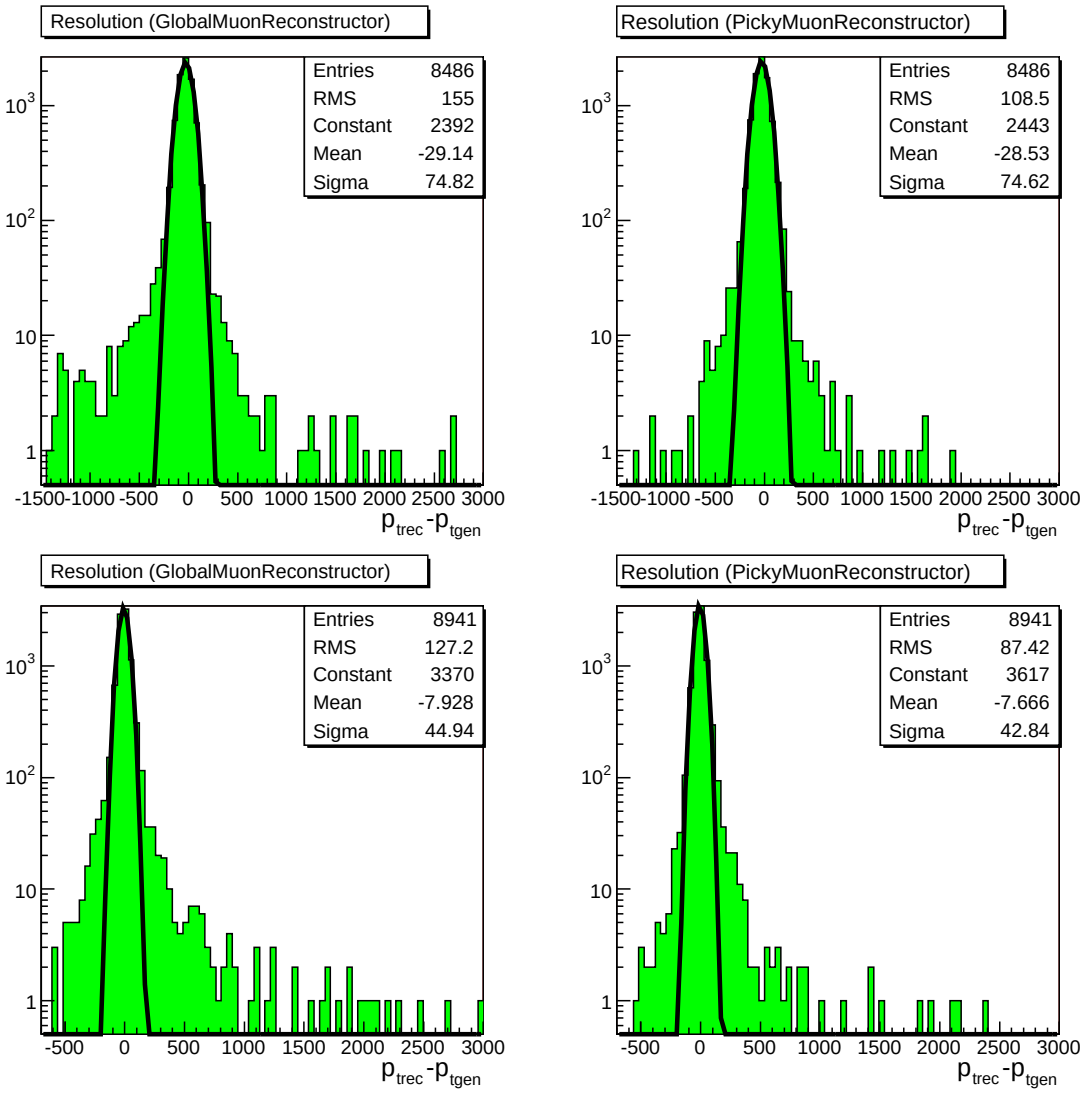


Figure 3.6: CMS momentum reconstruction resolution for 1500 GeV muons in the barrel (top) and endcap (bottom). The standard GlobalMuonReconstructor is shown on the left, and the modified version is on the right. A Gaussian is overlayed on the plots.

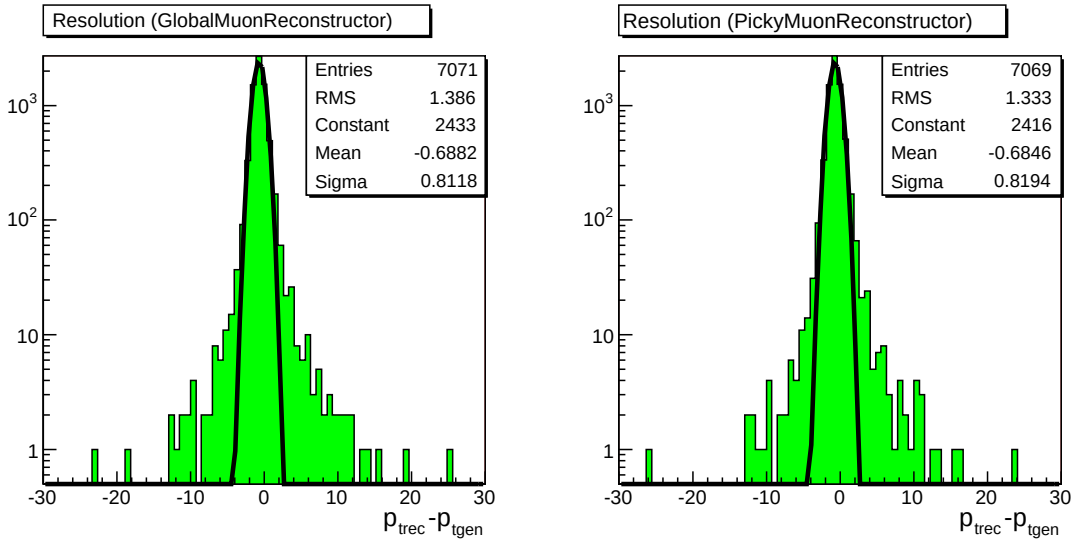


Figure 3.7: CMS momentum reconstruction resolution for 50 GeV muons. The standard GlobalMuonReconstructor is shown on the left, and the modified version is on the right. A Gaussian is overlayed on the plots.

| Sample | Algorithm | RMS | Effective efficiency |
|---|---|---|---|
| 1500 GeV muons, Barrel | GMR | 155 | 96.5% |
| | PMR | 109 | 98.1% |
| 1500 GeV muons, Endcap | GMR | 127 | 88.5% |
| | PMR | 87 | 91.0% |
| 50 GeV muons | GMR | 1.39 | 95.20% |
| | PMR | 1.33 | 95.24% |

Table 3.3: CMS muon reconstruction performance for the default (GMR) and optimized (PMR) algorithms.

### 3.3.2 Recovering bremsstrahlung photons

Additional corrections to the measured muon momentum can be obtained by looking in the electromagnetic calorimeter in the vicinity of the muon trajectory for photons radiated by the muon. Such photons come mainly from final state radiation from the graviton decay vertex, and can carry a significant fraction of the muon energy. Photons radiated by the muon in the CMS tracker can be also recovered this way, but they are usually low-energy and their effect on measured muon momentum is negligible.

This modification has been implemented as an extension of muon reconstruction - once a muon is reconstructed, the code looks for photons reconstructed in the ECAL (using the EgammaCandidate ORCA class) and selects the one closest to the muon in $\eta$-$\phi$ space. Information about the photon's reconstructed momentum and distance from the muon is then saved together with the information about the muon. This way, the decision what distance from the muon (cone size) to use, can be made during the final analysis stage. At that point, the photon associated with each muon is checked and if it falls into the cone, it's 4-momentum is added to the reconstructed muon's 4-momentum.

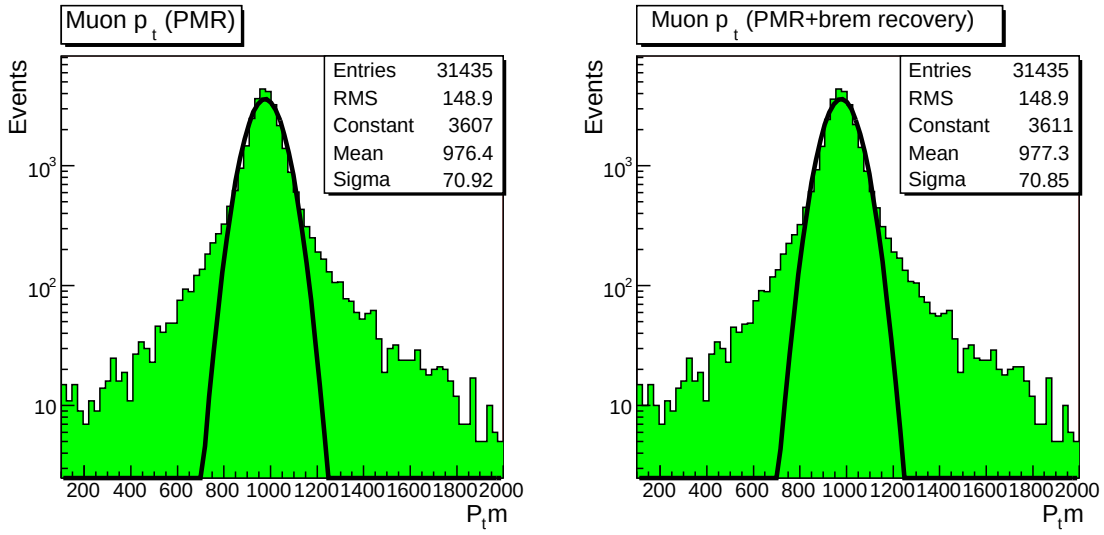


Figure 3.8: Reconstructed momentum of $p_t = 1000$ single muons. Events without correction are shown on the left, and the right plot shows the distribution after applying brem photon correction with a cone size of 0.1.

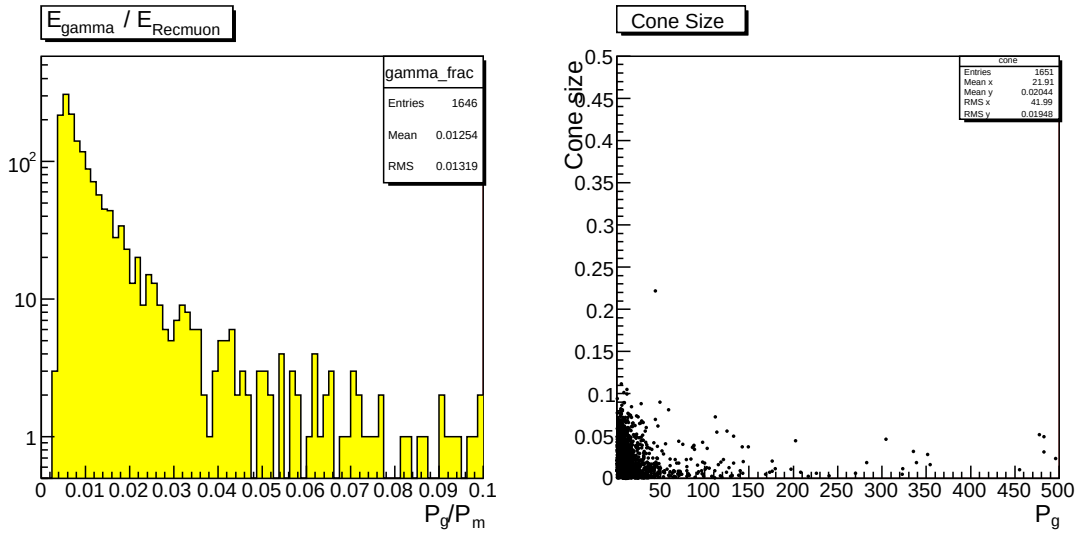


Figure 3.9: The left plot shows the fraction of muon energy carried by the reconstructed photon. The right plot is a scatter-plot of photon momentum vs its distance from the corresponding muon.

The cone size parameter was chosen after studying fully reconstructed samples of single muons and complete signal events. Analysis of 30 000 single muon events with muon $p_t = 1000$ GeV shows, that:

- only 5% muons radiated a photon before reaching the ECAL,
- the mean energy of the photons was 22 GeV (see Fig. 3.9),
- nearly 100% of the reconstructed photons fit in a 0.1 cone (Fig. 3.9),
- the mean reconstructed muon energy changes by $\sim$0.1% after adding the photons' energies (Fig. 3.8).

This shows that photon bremsstrahlung in the tracker doesn't have a significant impact on muon reconstruction. Analysis of a $G \to \mu\mu$ signal sample (with a graviton mass of 3 TeV) yields the following conclusions:

- a photon in a 0.1 cone was found for $\sim$10% of the muons,
- the mean photon energy was 161 GeV (Fig. 3.10),

- The photons radiated from the graviton decay vertex are effectively collinear with the muons, and a cone size of 0.1 gives good reproduction of the photon energy spectrum from Monte-Carlo.
- About 30% of low energy (less than 30 GeV) photons in a 0.1 cone are not coming from the graviton decay vertex,
- the effect of the correction on the mean reconstructed graviton mass is 1.5% (Fig. 3.11).

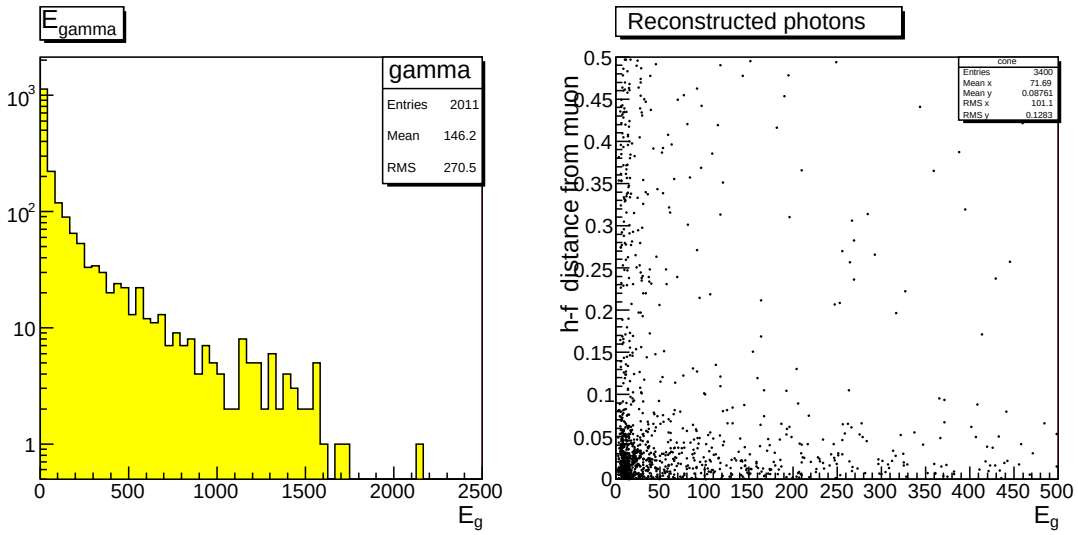


Figure 3.10: Reconstructed photons in a 0.1 $\eta$-$\phi$ cone, from 3 TeV $G \to \mu\mu$ signal sample. The left plot shows the photon energy spectrum, the right plot shows the photon energy and distance from the muon. Since for each muon the photon closest to it in $\eta$-$\phi$ is stored, to avoid plotting the same photon twice only photons associated with the first muon in each event are shown on the scatter plot.

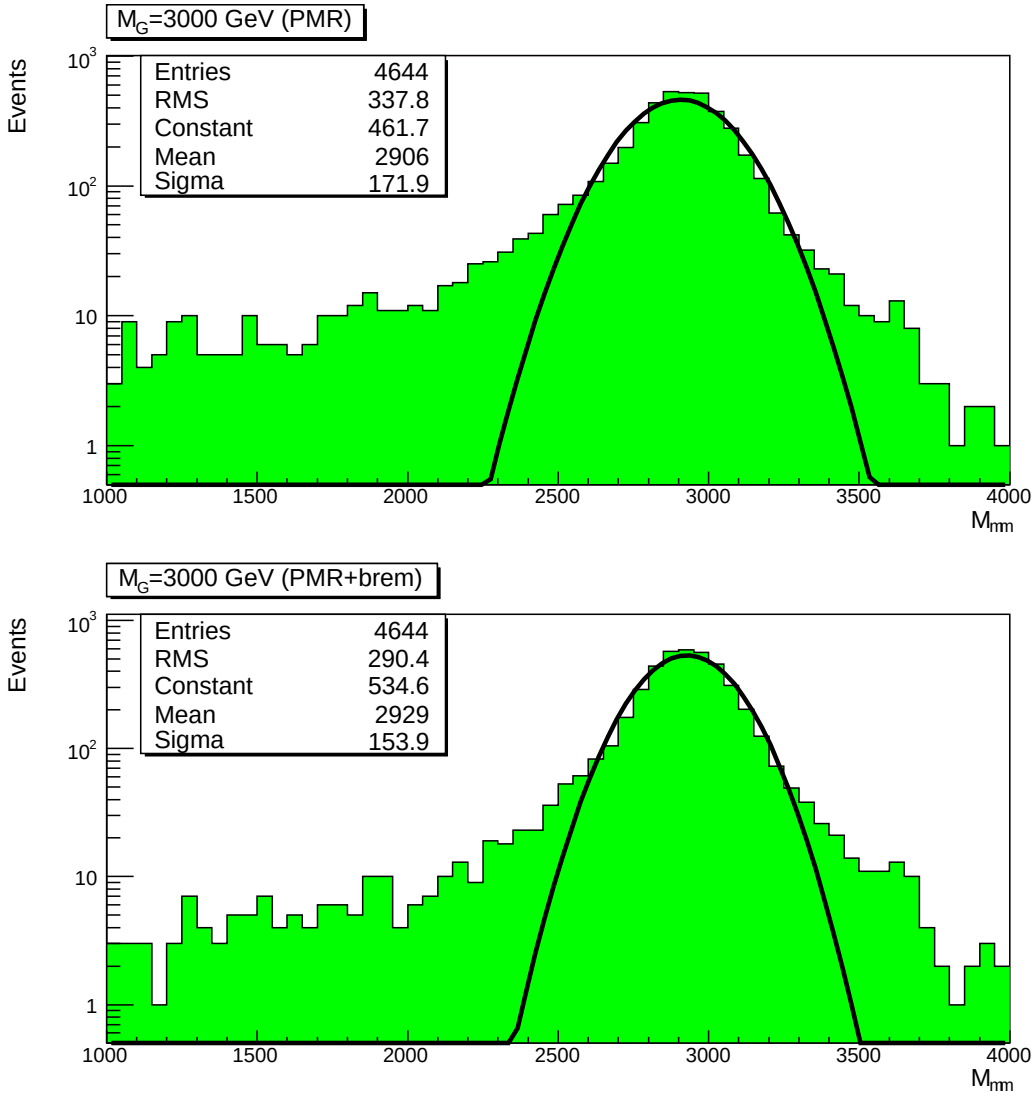


Figure 3.11: Reconstructed invariant mass spectrum of a $G \to \mu\mu$ signal sample. The top plot shows events without corrections, and the bottom plot shows the distribution after applying brem photon correction with a cone size of 0.1.

# Chapter 4

# Analysis

## 4.1 Method of discovering a TeV mass resonance

The most natural way to look for a new heavy resonance decaying into two muons is to analyze the invariant mass spectrum of muon pairs observed in the particle detector. There, a characteristic peak should be visible around the mass value of the hypothetical particle. In this analysis, the Standard Model background is continuous and exponentially falling, so the visibility of a peak with a given mass depends mainly on:

- the production cross-section times branching ratio for the dimuon decay channel, determining the signal to background ratio,
- the observed width of the resonance (dependent on the true width and on muon momentum measurement resolution),
- the collected integrated luminosity, determining the number of observed events and, in consequence, the significance level for the discovery (corresponding to the probability that the peak is only a statistical fluctuation of the background).

In the case of the Randall-Sundrum graviton, the width and the production cross-section are functions of the curvature parameter $k/M_{Pl}$, and the branching fraction into muons is fixed at 2.03%.

### 4.1.1 Discovery significance estimators

There exist two main classes of approaches to quantify the statistical significance of a signal in the presence of background. These are usually referred to as "event counting" and "likelihood" methods. The former use only two numbers to compute the significance level, namely the number of signal and background events in a "signal region" (for example an invariant mass window). The latter rely on fits of signal and background distributions to the data, extracting the significance level from the likelihood values in the best-fit point. For a review of some of the more common methods and their properties, see [43].

In this analysis signal observability was estimated by performing binned maximum-likelihood fits to reconstructed dimuon invariant mass spectrum and calculating the significance estimator

$$S_L = \sqrt{2\ln(\mathcal{L}_{s+b}/\mathcal{L}_b)} \tag{4.1}$$

where $\mathcal{L}_b$ and $\mathcal{L}_{s+b}$ are the best-fit likelihoods [1] of the probability density functions (pdf's) corresponding to the null hypothesis $H_0$ (no signal present) and the alternative hypothesis $H_1$ (signal plus background). The same method was applied in [44] to the search for $Z'$ bosons in the dimuon decay channel.

The interpretation of $S_L$ is given by the Wilks' theorem [45], stating that in case of the absence of signal, the distribution of $S_L^2$ in the large statistics limit is a $\chi^2$ distribution with the number of degrees of freedom (ndof) equal to the difference in the number of free parameters in $H_0$ and $H_1$ pdf's. If ndof difference is one, $S_L$ is expected to follow a standard Gaussian distribution with the mean in 0 and a standard deviation of 1. Hence, the probability of a pure background sample yielding a significance value higher than $N$ is equal to a one-sided Gaussian tail probability for $N$-$\sigma$, so the value of $S_L$ can be directly interpreted as the significance level of the test (given in the commonly used form of the "number of sigmas"). For example, a $S_L$ value of 5 (often referred to as the "discovery limit") corresponds to a $2.9 \times 10^{-7}$ probability that the signal is only a statistical fluctuation in the background (probability of a type-1 error - rejecting $H_0$ when it is true).

[1] The likelihood of a data sample under a given hypothesis, given it's pdf, is defined as the product of probabilities of all events in the sample. $\mathcal{L} = \prod_{x \in datatset} pdf(x)$

The pdf used in the fit

$$p(M_{\mu\mu}; N_S, M_G, \Gamma, k) = N_S \cdot p_G(M_{\mu\mu}; M_G, \Gamma, \tau) + N_B \cdot p_{DY}(M_{\mu\mu}; k, a, b, f) \quad (4.2)$$

is a sum of signal and background pdf's. The background-only hypothesis is simulated by fixing the number of events $N_S = 0$.

The notation is as follows:

The signal pdf $p_G$ is a convolution of a negative Landau distribution modeling the radiative tail with a Gaussian accounting for the graviton width and mass reconstruction resolution (see Fig. 4.1):

$$p_G(M_{\mu\mu}; M_G, \Gamma, \tau) = Landau(-M_{\mu\mu}; -M_G, \tau) \otimes Gauss(M_{\mu\mu}; M_G, \Gamma) \quad (4.3)$$

where:

- $M_G$ is the mass of the resonance. In the fits it was fixed at a value obtained from a fit to the signal-only distribution.
- $\Gamma$ is the width of the Gaussian accounting for the resonance width and muon momentum resolution tail. Currently is it also obtained from a fit to the full-statistics signal sample.
- $\tau$ is the width of the Landau distribution modeling the radiative tail. Fits to generator-level pure signal samples have shown that a value of $0.006 \cdot M_G$ is a good approximation, so this number was used throughout the analysis[1].

In order to keep the ndof difference of 1 between the two hypotheses all the parameters of the signal pdf were fixed.

The background pdf is given as a sum of two exponents (two exponents are needed when fitting the background shape over a broad range of invariant masses - see Fig. 4.2):

$$p_{DY}(M_{\mu\mu}; k, a, b, f) = (1 - f) \cdot e^{-(k \cdot M_{\mu\mu})} + f \cdot e^{-a \cdot M_{\mu\mu} + b \cdot M_{\mu\mu}^2} \quad (4.4)$$

where:

[1] As is discussed in Section 4.5, this parameter has only a small impact on signal significance.

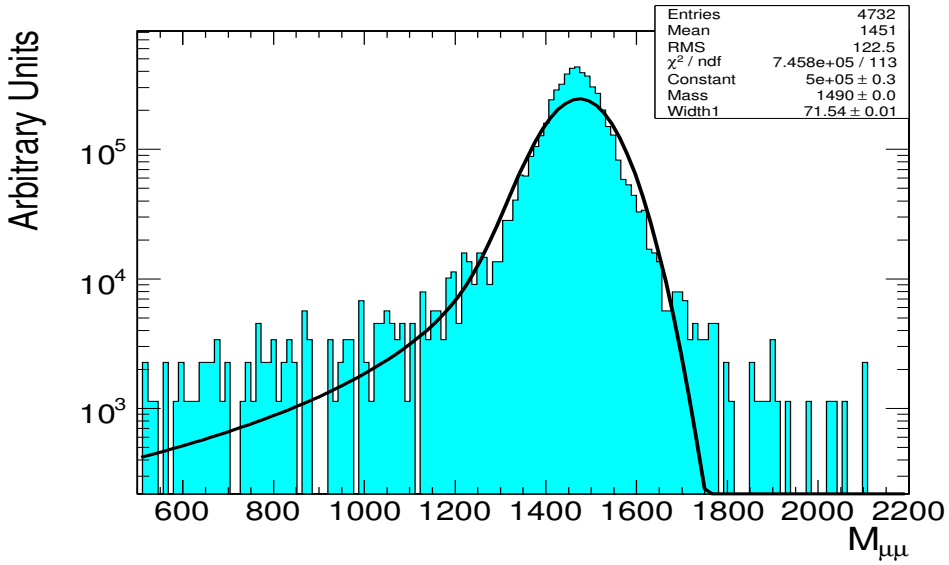


Figure 4.1: Reconstructed invariant mass distribution for a pure signal sample, with the signal pdf fit overlayed. A graviton with mass 1.5 TeV and $c = 0.01$ is plotted, the normalization is arbitrary.

- $f$ is the ratio of the two components.
- $k$ is the slope of the falling Drell-Yan spectrum for masses above 1.5 TeV.
- $a$ is the slope for masses below 1 TeV.
- $b$ is an additional quadratic term, added to better reproduce the Drell-Yan shape.

The values of the background pdf parameters were obtained from fits to the full background only sample and fixed during the fit. Other ways of determining these parameters were also explored and are discussed below. The quadratic term $b$ starts becoming significant when describing the Drell-Yan spectrum for high masses (above 3 TeV), where only single events are expected, even for $100 fb^{-1}$ integrated luminosity. The statistical uncertainties in this region are high, making the determination of $b$ from data problematic. Moreover, including and omitting this term was found to have a very small effect on the results of the fits (from no change for low graviton mass up to 7% for 4 TeV gravitons), so the analysis was done with its value fixed at zero.

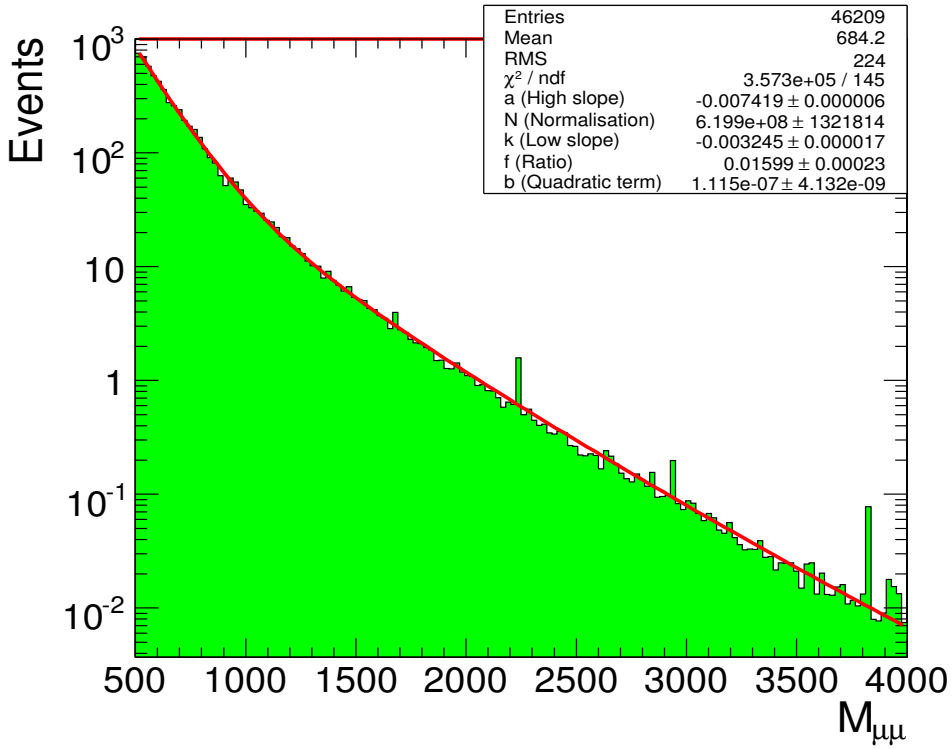


Figure 4.2: Reconstructed invariant mass distribution for the Drell-Yan background process, with the background-only pdf fit overlayed. The plot corresponds to 100 fb$^{-}$1 of integrated luminosity. The single spikes visible in the plot are events with highly over-estimated reconstructed momentum of one of the muons. They have larger weights than neighboring events, since they come from different generated $\hat{p}_t$ bin (see Fig. 3.1).

### 4.1.2 Toy Monte-Carlo tests of significance estimators

In order to accurately report a 5 sigma significance level, one has to check the tails of the background-only $S_L$ distribution, since the asymptotic behavior guaranteed by the Wilks' theorem may not be realized in a small statistics case. The distributions of the significance estimator in this analysis were studied by generating sets of random pseudo-experiments (toy Monte-Carlo).

The results for 10000 simulated events, for a 1500 GeV graviton with coupling $c = 0.01$, are shown in Fig. 4.3. Plots for other sets of Randall-Sundrum model parameters are similar, in particular for all cases it can be noted that:

- the distribution for the case with no signal is consistent with a standard Gaussian.
- the distribution for the case when a signal is present is also Gaussian, with the standard deviation close to 1 and mean within 5% of the $S_L$ value obtained from fits to the full MC samples.

The main conclusion from this is that the mean significance level can be calculated by performing the analysis on the full generated samples, without the need for toy Monte-Carlo. This mean significance is then reported as **the** expected significance in the experiment. This means that in a real experiment the chance of achieving such significance level is 50% - this widely used interpretation of the result corresponds to setting type-II error probability[1] of the test at 0.5.

To study the $5\sigma$ tail of the background-only distribution, a test with larger statistics has to be performed to check if the probability of observing $S_L > 5$ is indeed consistent with $2.9 \times 10^{-7}$. A result of such a test is shown in Fig. 4.4. As can be seen from the plot, the behavior of the significance estimator is in very good agreement with theoretical predictions. Four events appeared above the value of 5, corresponding to a $5 \times 10^{-7}$ probability. This confirms the validity of the usage of the $S_L$ estimator for $5\sigma$ searches in this analysis.

[1] the probability of accepting the null hypothesis $H_0$ when it is false - missing a true signal.

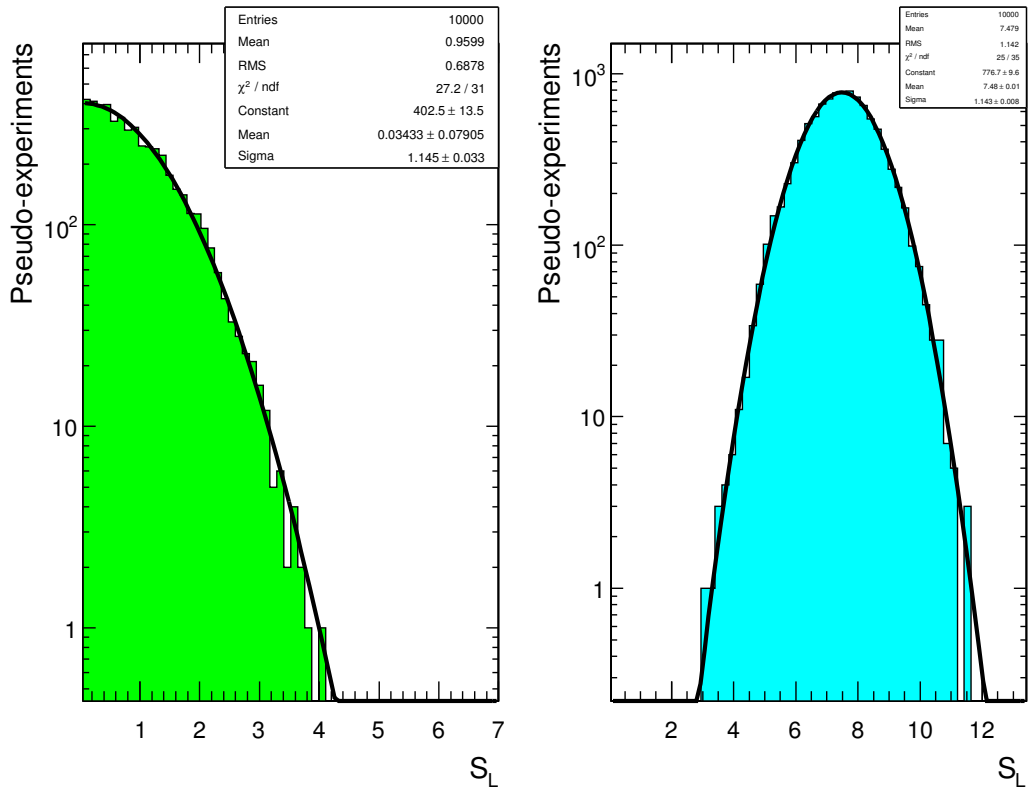


Figure 4.3: Distributions of $S_L$ values obtained in fits to 10000 simulated pseudo-experiments. The case when only the Drell-Yan background was present is shown on the left plot, the right plot shows the results for a 1500 GeV graviton. The curves represent Gaussian fits to the histograms.

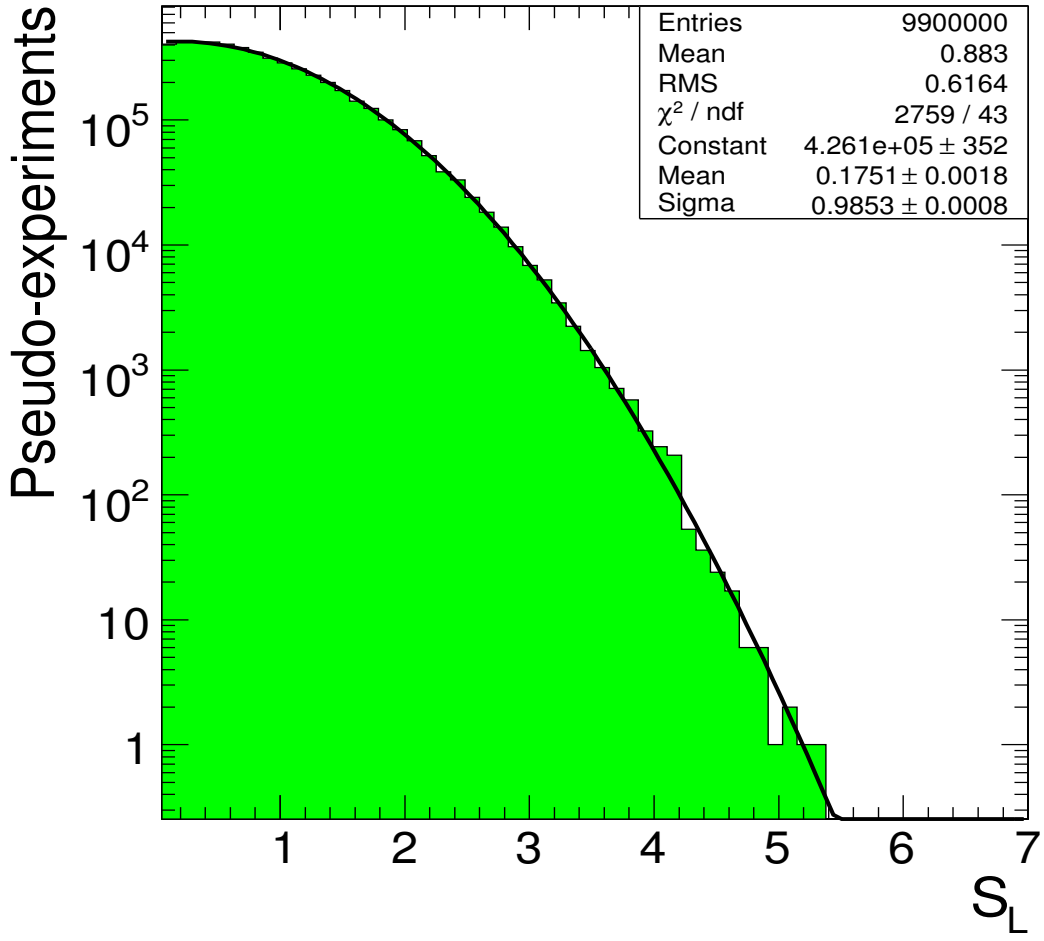


Figure 4.4: Large statistics (10 million) toy Monte-Carlo test of $S_L$ behavior for a background-only data sample, with a Gaussian fit overlayed.

## 4.2 Method of determining the spin of the observed particle

Once a new heavy particle has been discovered, one has to determine it's properties and identity. The characteristic feature of the massive graviton is it's spin. The graviton has spin 2, as opposed to other heavy neutral bosons, which have spin 1.

The spin of the observed resonance manifests itself in the angular distributions of its decay products (see also Fig. 4.5):

| subprocess | angular distribution |
|---|---|
| $q\bar{q} \to \gamma/Z^0/Z' \to f\bar{f}$ | $\frac{3}{8}(1+\cos\theta^{*2})$ |
| $q\bar{q} \to G^* \to f\bar{f}$ | $\frac{5}{8}(1-3\cos\theta^{*2}+4\cos\theta^{*4})$ |
| $gg \to G^* \to f\bar{f}$ | $\frac{5}{8}(1-\cos\theta^{*4})$ |

where $\cos\theta^*$ is the angle between the incident quark or gluon and the outgoing lepton in the dimuon center-of-mass frame. In an experimental situation the transverse momenta of the incoming partons are not known, in such a case optimal results are achieved by calculating $\cos\theta^*$ in the Collins-Soper frame [46], in which the reference axis is the axis bisecting the target and beam directions measured in the dimuon center-of-mass frame. In order to reduce the contamination from the Drell-Yan background, only events in a $\sim 2\sigma$ mass window around the resonance peak are considered in this analysis. The window width was optimized to provide the best level of discrimination between the tested hypotheses. As a result, a width equal to 2 times the width of the Gaussian fitted to the resonance peak was chosen. The generated and reconstructed angular distributions for 3 TeV resonances are shown in Fig. 4.6.

The problem of determining the spin of the observed particle is, as in the case of the mass reach, a problem of rejecting one spin hypothesis $H_1$, thus accepting the alternative $H_2$. [1] In a search for a Randall-Sundrum graviton, one is tempted to treat spin-1 as the null "background-only" hypothesis and repeat the reasoning

[1] This is of course true only in a two hypothesis case. Since most current theoretical predictions for a very massive di-lepton resonance are spin-1 or spin-2 particles, other options (for example spin-0) are not considered here.

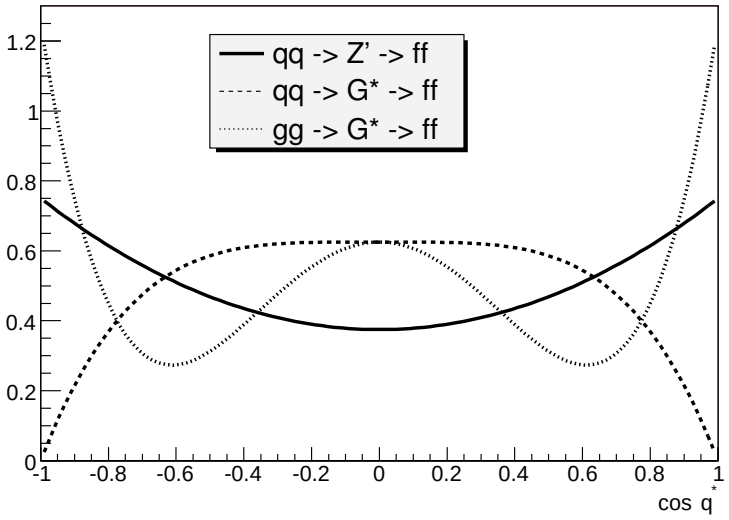


Figure 4.5: Theoretical angular distribution shapes for spin-1 and spin-2 resonances.

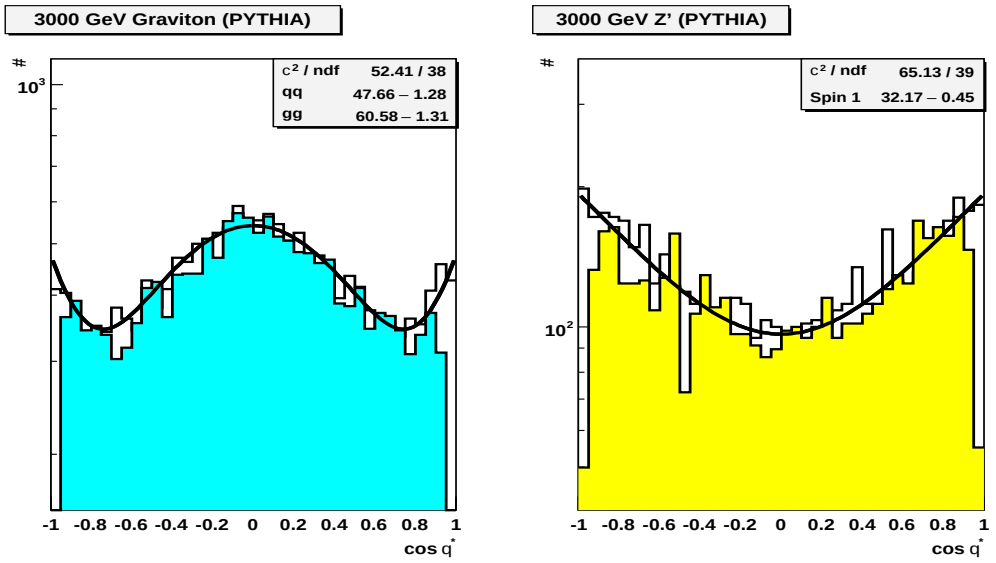


Figure 4.6: Angular distributions for 3000 GeV generated graviton (left) and $Z'$ (right). Open histograms correspond to generator-level data, while the colored histograms show events after full detector simulation and reconstruction. Theoretical curves fit to the Monte-Carlo data are overlayed.

from Section 4.1 with angular distributions in the place of invariant mass spectra. This approach is, however, asymmetric in the treatment of the two hypotheses: as was discussed above, spin-1 exclusion with a given significance level, claimed on the basis of this test, will only happen in a real experiment with a 50% chance.

In order to treat the two hypotheses on a more equal footing, following [47] we construct a test with equal probabilities of type-1 and type-2 errors. In a case when the $S_L$ distribution is Gaussian for both $H_1$ and $H_2$ (with means $m_1$, $m_2$ and sigmas $\sigma_1$, $\sigma_2$ respectively), this corresponds to finding $x$ such that

$$m_1 + x \cdot \sigma_1 = m_2 - x \cdot \sigma_2 \ .$$

Note that this reasoning does not affect the interpretation of $S_L$ once data is in hand, it only applies to quantifying the expected sensitivity of a planned experiment. Real data will give a certain value of our test statistic, and it can/will be converted to the significance level.

The test statistic used to distinguish the two hypotheses is the likelihood ratio:

$$-2\ln\lambda = 2\ln\frac{\mathcal{L}_1}{\mathcal{L}_2} \tag{4.5}$$

Where $\mathcal{L}_1$ and $\mathcal{L}_2$ are unbinned likelihood values for the data sample under the two hypotheses considered (spin-1 and spin-2, respectively). The pdf used for the likelihood calculation has the form

$$p(\cos\theta^*) = N_1 \cdot p_1(\cos\theta^*) + N_{q\bar{q}} \cdot p_{q\bar{q}}(\cos\theta^*) + N_{gg} \cdot p_{gg}(\cos\theta^*) \tag{4.6}$$

where $N_1 + N_{q\bar{q}} + N_{gg} = 1$ are the relative contributions from the spin-1 and the two spin-2 subprocesses. The spin-1 hypothesis corresponds to $N_1 = 1$ and the spin-2 hypothesis corresponds to fixing all the parameters according to the ratio of the $q\bar{q}$ and $gg$ graviton production processes and signal-to-background ratio in the mass window.

Since this is a case with no free parameters, the likelihood ratio for a data sample is simply a sum of contributions from all the events. The likelihood of each event should in principle be multiplied by as acceptance function $f(\cos\theta^*)$ to account for the difference in shape between the predicted and reconstructed

angular distributions (due mainly to the muon geometrical acceptance in CMS). This function however, is independent of the angular distribution itself, so in the ratio of the two likelihoods it simply cancels.

Fig. 4.7 shows the distributions of the individual contributions for the full sample of signal and background events reconstructed in the mass window, for a 1000 GeV graviton and $Z'$. A real experiment corresponds to selecting the appropriate number of events $N$ from this distribution and adding the $-2\ln\lambda$ values. In such a case, the Central Limit Theorem implies that the value of $-2\ln\lambda$ should follow a Gaussian distribution with mean and sigma calculated by scaling the mean and RMS values of the histograms in Fig. 4.7 by $N$ and $\sqrt{N}$, respectively. This is indeed so, an example plot for 1000 GeV resonance mass is shown in Fig. 4.8.

The significance level can be calculated for each set of simulated model parameters, either by running toy Monte-Carlo taking the means and widths of the Gaussians for $H_1$ and $H_2$ from fits to the distributions of $-2\ln\lambda$, or by simply rescaling the mean and RMS of histograms with all reconstructed events in the mass window. The results agree within 5%, and so latter method was used.

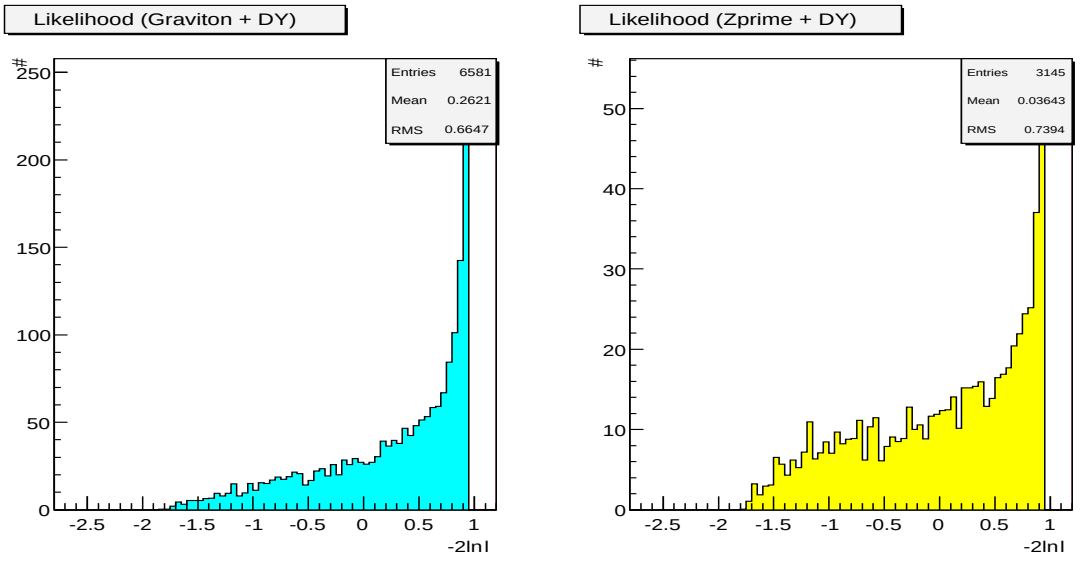


Figure 4.7: Contributions to the likelihood function (Eq. 4.5) from individual simulated events, for a 1000 GeV graviton (left) and $Z'$ (right), with the Drell-Yan contribution added.

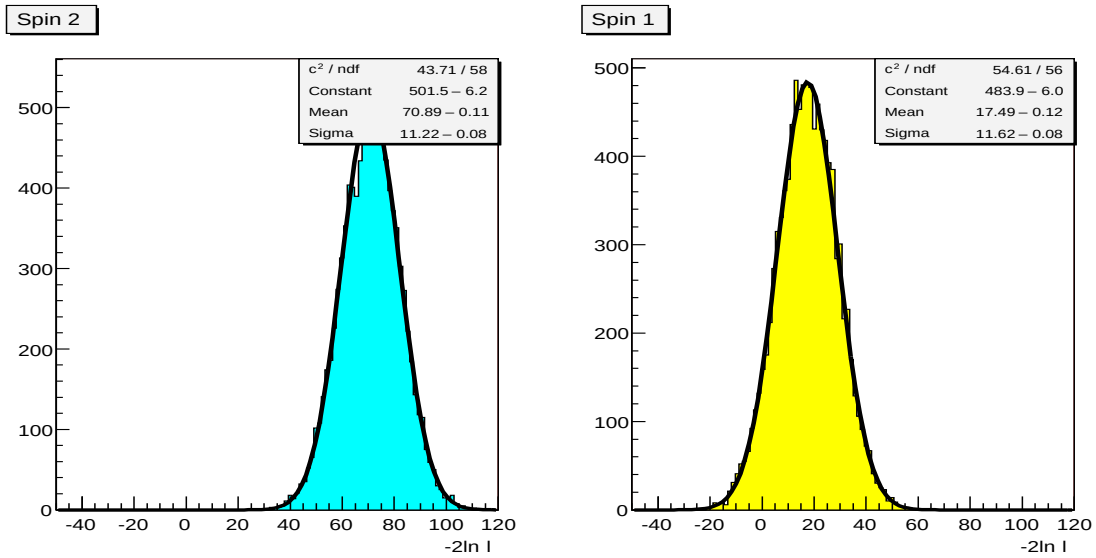


Figure 4.8: Values of $-2\ln\lambda$ obtained in 10000 pseudo-experiments, for a 1000 GeV graviton (left) and $Z'$ (right).

## 4.3 Other methods of distinguishing between the G and the $Z'$

Analyzing angular distribution it not the only way to distinguish between the graviton and a $Z'$. In general, two types of methods can be used: a global analysis across different channels or experiments, or a more complex analysis within one channel. The first type can involve studying other decay processes and comparing their branching ratios with theoretical predictions. For example diphoton decay, which gives a very promising discovery channel for the RS graviton, is absent in the case of a neutral $Z'$ - in the first order these particles don't couple to photons. This kind of analysis in not considered in this work, however.

Another possible approach is to study other kinematic variables, besides $\cos\theta^*$. For example, transverse momentum of the dimuon system is expected to have different behavior for graviton and $Z'$ [48].

The distributions of $p_t$ of the produced resonance are shown in Fig. 4.9. The graviton tends to have a higher $p_t$ than the $Z'$. This is due to the additional production process of gluon fusion, gluons are expected to have a harder $p_t$ spectrum

due to larger initial state radiation [48]. In order to make use of this difference in the analysis, a two-dimensional likelihood function was constructed, taking into account both the angular and $p_t$ information. Due to the lack of theoretical predictions for the functional form of the pdf's, a binned likelihood function was used, with the pdf's taken from full reconstructed data samples. An example of the pdf's used for the two hypotheses under study (a graviton and a $Z'$) is shown in Fig. 4.10.

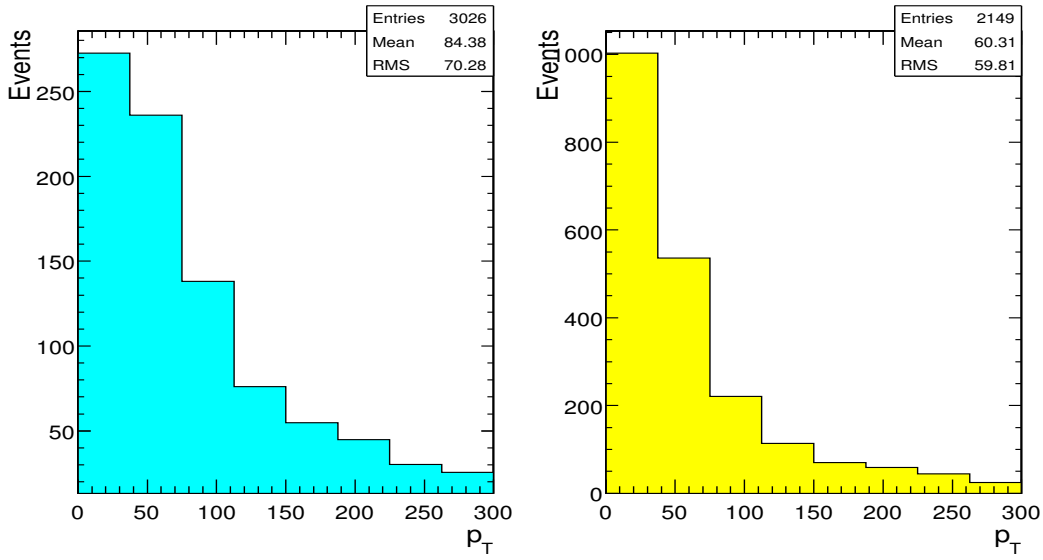


Figure 4.9: Transverse momentum of the dimuon system for a 1 TeV graviton (left) and $Z'$ (right).

The rest of the analysis is analogous to the one-dimensional analysis of Section 4.2. The distributions of individual contributions to the likelihood ratio from each generated event are shown in Fig. 4.11. The histograms are much less continuous that in the previous case (Fig. 4.7) - this is a consequence of using histograms instead of analytical functions as pdf's. This doesn't spoil the convergence to Gaussians, as can be seen from Fig. 4.12. The significance can be thus calculated as above, by appropriately scaling the mean and RMS values of the histograms in Fig. 4.11.

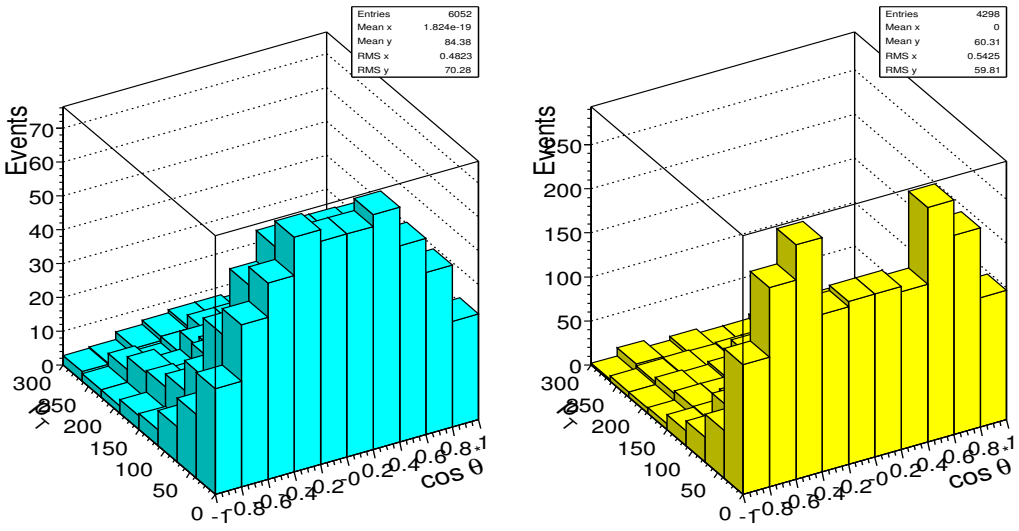


Figure 4.10: Two-dimensional plots of the dimuon $p_t$ and $cos\theta^*$ distributions for a 1000 GeV graviton (left) and $Z'$ (right).

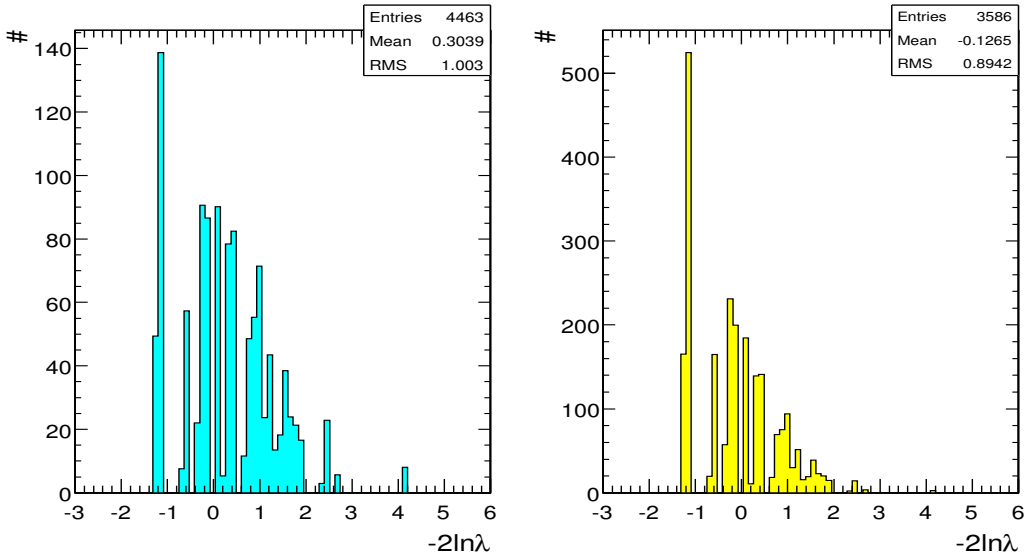


Figure 4.11: Contributions to the 2D ($p_t$ and $cos\theta^*$) likelihood function from individual simulated events, for a 1000 GeV graviton (left) and $Z'$ (right), with the Drell-Yan contribution added.

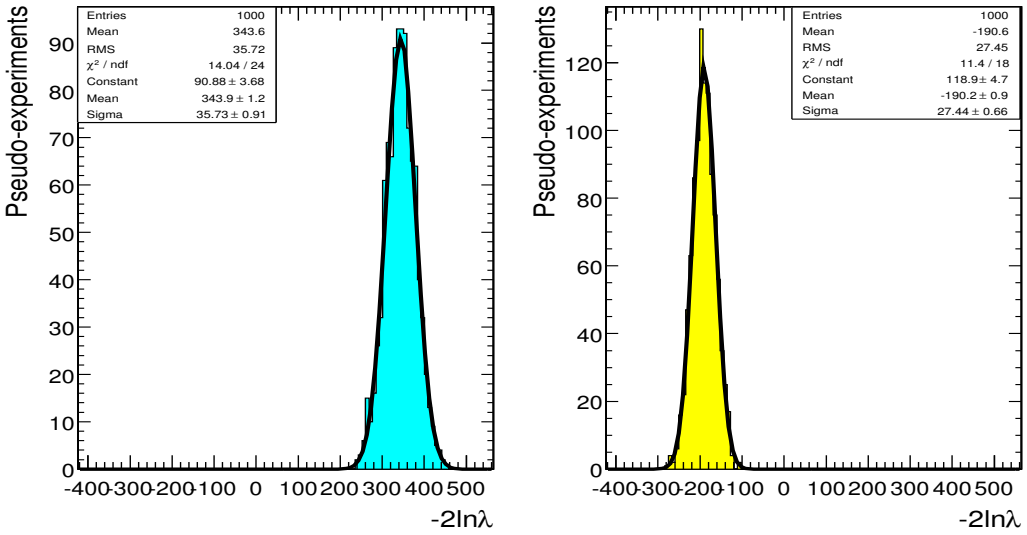


Figure 4.12: Values of $-2\ln\lambda$ obtained in 10000 pseudo-experiments, for a 1000 GeV graviton (left) and $Z'$ (right).

## 4.4 Results

### 4.4.1 $5\sigma$ Discovery reach

In order to plot the $5\sigma$ reach contours the logarithms of $S_L$ values obtained for different graviton masses were fitted with a quadratic function, independently for each considered value of $k/M_{Pl}$. This parameterization was used to calculate the mass values corresponding to $5\sigma$. The result is plotted in Fig. 4.13, for 10 fb$^{-1}$ and 100 fb$^{-1}$ integrated luminosity. As can be seen from the plot, the whole interesting region is accessible after collecting 100 fb$^{-1}$ of data.

### 4.4.2 Resonance mass measurement

The relative error on the fitted mass, measured as $(M_{rec}-M_{gen})/M_{gen}$, is shown in Fig. 4.15 ($M_{rec}$ is the mean reconstructed mass value from 300 simulated pseudo-experiments, averaged over all the simulated signal samples with the same mass, and $M_{gen}$ is the graviton mass chosen in simulation). The plot shows the effect of different functional form of the signal shape used in the fit (pure Gaussian or

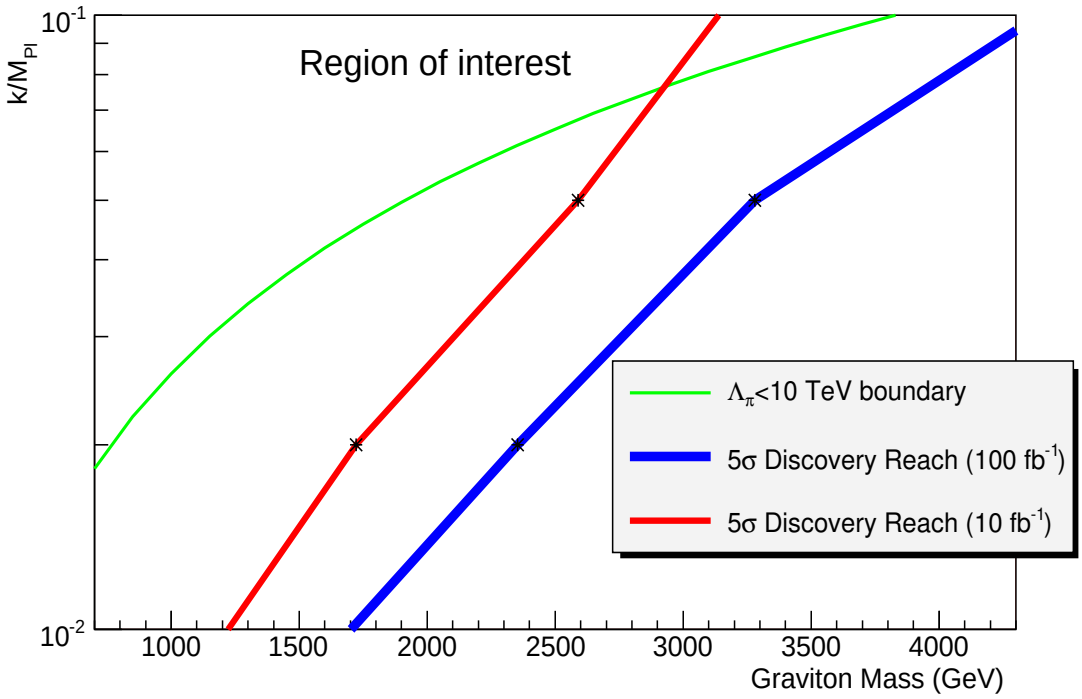


Figure 4.13: CMS reach for $5\sigma$ discovery of the Randall-Sundrum graviton. The area to the left of the curves is the region expected to be probed in the CMS experiment.

Gaussian-Landau convolution) - taking into account the radiative tail significantly lowers the difference between the reconstructed mass and the true value. Correcting the muon momentum measurement with reconstructed bremsstrahlung photons also gives a sizable improvement - the final reconstructed mass value is underestimated by only ∼1%.

The precision of the mass fit is illustrated in Fig. 4.14, where the values obtained in 300 simulated pseudo-experiments are shown, along with a Gaussian fit to the distribution. This fit was repeated for all of the simulated signal samples. The precision of the fit for all simulated signal datasets, calculated as the width of the Gaussian fit to the $M_{rec}$ distribution divided by $M_{gen}$, is shown in Fig. 4.16. Fits with the full signal pdf and with photon recovery have better precision than uncorrected fits with simple Gaussian. For a constant value of the graviton coupling the fit precision drops with increasing graviton mass, due to the decreasing number of signal events. At the point where the precision is 5% it's estimation starts behaving in an erratic way, partially due to the small statistics of toy Monte-Carlo.

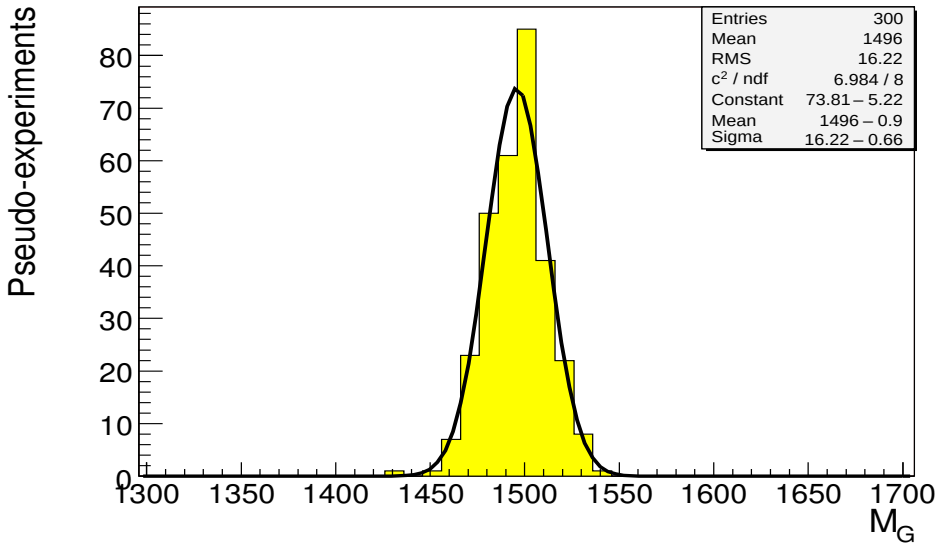


Figure 4.14: Reconstructed graviton mass distribution for a graviton with mass equal to 1500 GeV and $c = 0.01$. The plot shows results from 1000 toy Monte-Carlo experiments, with a Gaussian fit overlayed.

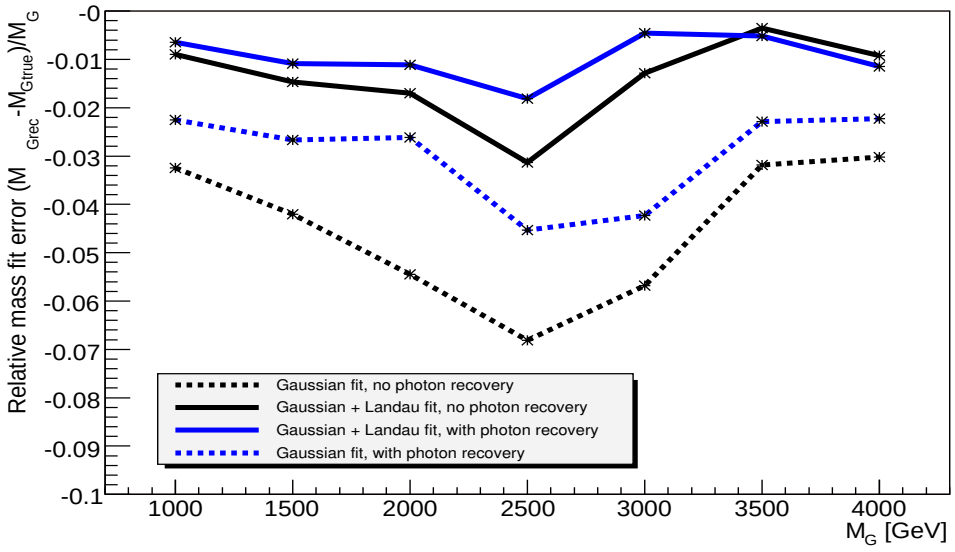


Figure 4.15: Relative error on reconstructed graviton mass, averaged over the points with different coupling. Solid lines correspond to results fitted with Gaussian convoluted with a Landau (Eq.4.3), dashed lines correspond to fit with a Gaussian pdf. Blue lines show results with photon recovery turned on (see Section 3.3.2), black lines show results without photon recovery.

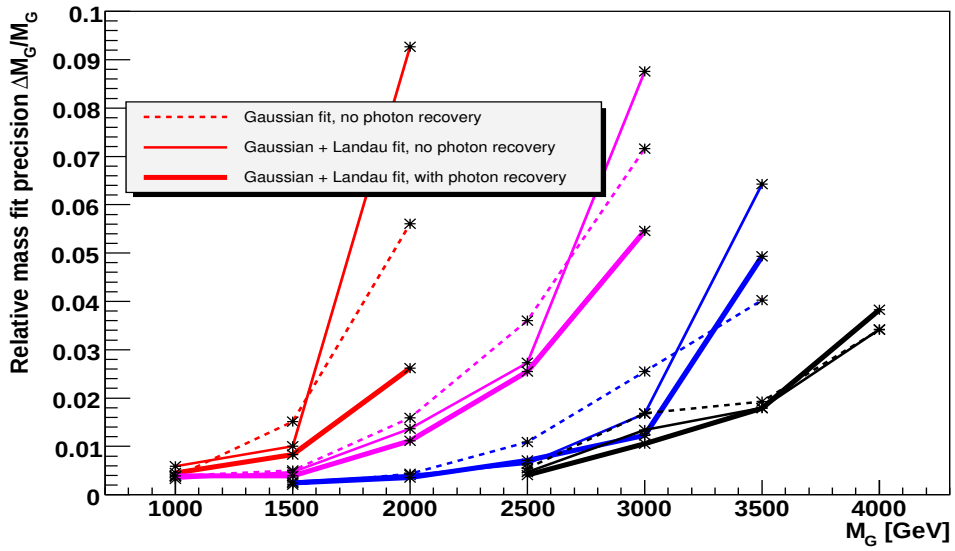


Figure 4.16: Relative precision of the graviton mass fit. Different colors correspond to different values of the coupling parameter $k/M_{Pl}$ (from left to right: 0.01, 0.02, 0.05, 0.10). Solid lines correspond to results fitted with Gaussian convoluted with a Landau (Eq.4.3), dashed lines correspond to fit with a Gaussian pdf. Thick lines show the effect of turning on photon recovery (see Section 3.3.2).

### 4.4.3 Establishing the identity of the observed particle

The CMS reach for $2\sigma$ discrimination between the graviton and the $Z'$ in the $M_G$ - $k/M_{Pl}$ plane is shown in Fig. 4.17 for the angular distribution analysis. The result of the analysis with $p_t$ information added in the fit is shown in Fig. 4.18. As can be seen from the figures, expanding the likelihood function to include dimuon transverse momentum gives a clear improvement in the experimental reach. This result has to be treated with caution however, due to strong dependence on Monte-Carlo. The $p_t$ distributions of partons have large theoretical uncertainties, especially for the energies considered here. The two-dimensional analysis results should be interpreted as an indication of possible gain from using $p_t$ information to distinguish the graviton from a $Z'$.

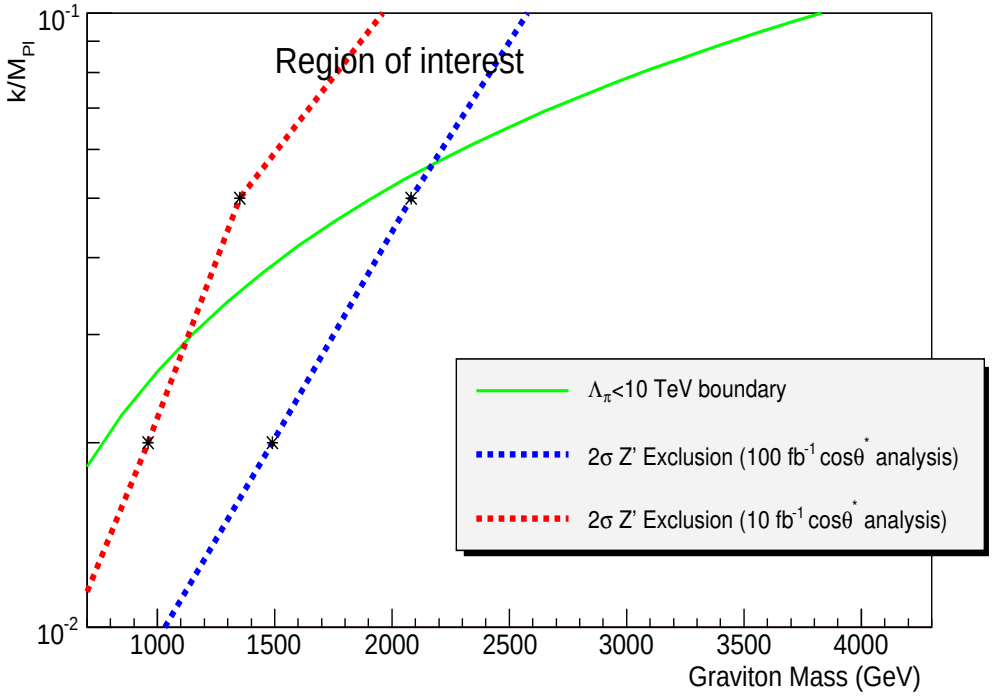


Figure 4.17: CMS reach for $2\sigma$ discrimination between spin-1 and spin-2 hypotheses for different integrated luminosities, based of angular distributions. The region to the left of the curves is the region where spin-1 can be excluded on a $2\sigma$ level.

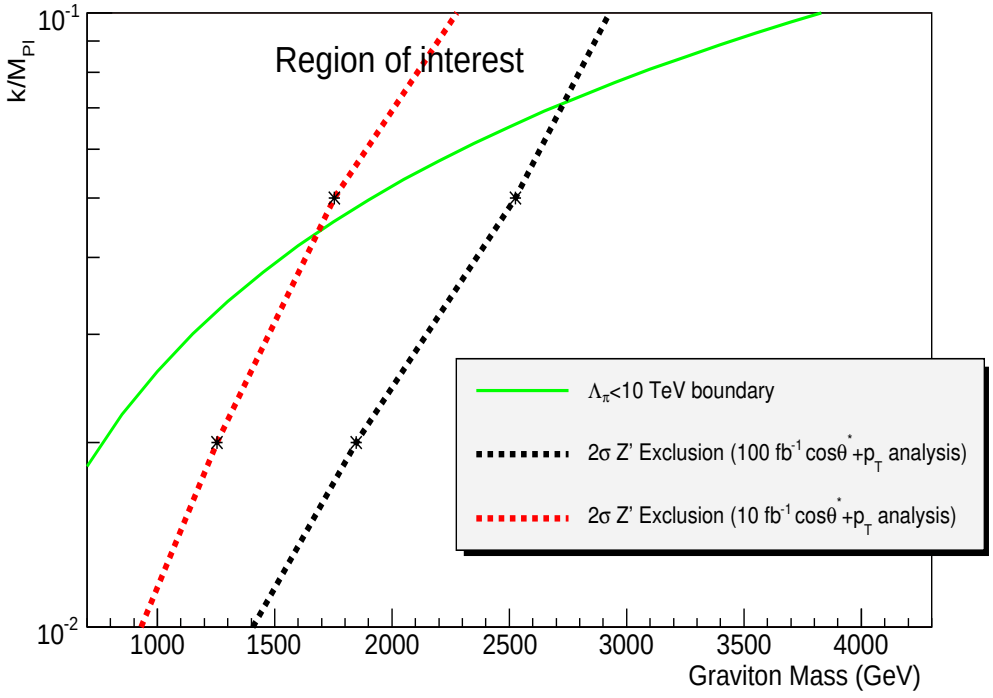


Figure 4.18: CMS reach for $2\sigma$ discrimination between a graviton and a $Z'$ for different integrated luminosities, with both angular and $p_T$ distributions used in the analysis. $2\sigma$ exclusion of the $Z'$ hypothesis is possible in the region to the left of the curves.

## 4.5 Systematic uncertainties

In an analysis based purely on Monte-Carlo there are two types of systematic uncertainties that need to be taken into account. The first one is a consequence of our limited knowledge of physics in the yet-unexplored energy region of the LHC. This includes parton distribution function (pdf), hard process scale uncertainties and higher order QCD and electroweak corrections. These uncertainties will likely be absent or negligible in a working experiment, so they only affect the *expected* experimental reach - for example different pdf's can yield different numbers of signal and background events in the signal region, leading to a change in significance. In reality however, only one of them is correct, and by the time 10 $\text{fb}^{-1}$ of data is collected, it will be known with good precision. An analysis designed to be applied to real data should be independent of these variations.

The second type of systematic uncertainties are uncertainties resulting from imperfect knowledge of the detector and those inherent in the analysis itself. The effects of the former (including pileup, tracker and muon system misalignment, and magnetic field uncertainty) have been studied elsewhere [49]. They were found to be negligible, with the exception of misalignment, which had the effect of reducing the $5\sigma$ reach in graviton mass by $\sim$100 GeV, taking into account expected performance of the CMS alignment system after about one year of data taking. The uncertainties resulting directly from the analysis procedure are mainly due to assumptions about the properties of the signal and background.

In order to keep the difference in the number of free parameters between the signal+background and background only pdf's equal to one, the mass and width of the resonance were fixed in the fit. The logic behind this is different in each of the two cases:

- The resonance width is governed by two parameters in the fit: the width of the Landau function and the FWHM of the Gaussian. The Landau function accounts mainly for the radiative tail, fixing the Landau width at zero affects only the mass fit – the mean reconstructed graviton mass is lower by $\sim$3% and the significance remains unchanged. The Gaussian width is a combination of the resonance width and the muon momentum resolution width. These are assumed to be known with sufficient precision -

it was checked that a 30% increase or decrease in the assumed width changes the final significance by ∼1%.

- The mass of the new particle can be determined by "scanning" the Drell-Yan continuum with fits with different mass hypotheses (this is essentially equivalent to doing a fit with the mass as a free parameter). The interpretation of $S_L$ in terms of discovery significance in such a case changes, since the difference in the number of free parameters between $p_G$ and $p_{DY}$ becomes two when the graviton mass is fitted. The value of $M_G$ maximizing signal likelihood corresponds to a hypothetical particle which is least probable to be a background fluctuation, but an excess of events appearing anywhere in the invariant mass spectrum is more probable than an excess appearing in a set region.

Fixing the parameters of the background pdf does not in principle affect the interpretation of $S_L$ since this pdf appears in both $H_1$ and $H_2$ fits and the difference in the number of free parameters is not affected. Freeing the background parameters is however not a good choice since it makes the fit unstable and reduces the signal significance by $\sim 20\%$. In a real experiment it might be necessary to extract some or all of the background shape parameters from the data, depending on the level of trust in the Monte Carlo estimates. This is best done by fitting the background pdf in signal-free regions. The exact strategy depends on the graviton mass and on the amount of data available. For low-mass resonances (of the order of 1 TeV), the background can be approximated with a single exponent, and the slope can be obtained from a fit to the left sideband of the invariant mass spectrum. For large integrated luminosity, information can also be extracted from the region to the right of the resonance. For gravitons with masses above 2 TeV fits in the left sideband give a good approximation of the background parameters.

Such a procedure has the advantage of being largely independent of Monte-Carlo – if in reality the background has a different slope or normalization than assumed in the present analysis, the results will be different, but will remain valid. The price to pay for this is a $\sim 10\%$ reduction in signal significance (with respect to the ideal case where background shape is taken from MC) and additional

statistical uncertainty – the FWHM of the $S_L$ distribution changes to a value of $\sim 1.5$, from $\sim 1$ in the ideal case.

## 4.6 Conclusions

The above analysis shows the prospects for observing massive excited graviton stated predicted by the Randall-Sundrum model in CMS. After collecting $100\,\mathrm{fb}^{-1}$ of the Randall-Sundrum graviton can be discovered by the CMS experiment in the whole interesting region of model parameters. It can be distinguished from a spin-1 particle up to masses of 1-2.5 TeV, depending on the coupling. The results are summarized in Table 4.1.

| | | Graviton mass reach [TeV] | |
|---|---|---|---|
| $k/M_{Pl}$ | | 10 fb$^{-1}$ | 100 fb$^{-1}$ |
| 0.01 | $5\sigma$ discovery | 1.22 | 1.70 |
| | $2\sigma$ spin disc. (1D) | 0.64 | 1.03 |
| | $2\sigma$ spin disc. (2D) | 0.93 | 1.41 |
| 0.02 | $5\sigma$ discovery | 1.72 | 2.35 |
| | $2\sigma$ spin disc. (1D) | 0.96 | 1.49 |
| | $2\sigma$ spin disc. (2D) | 1.25 | 1.85 |
| 0.05 | $5\sigma$ discovery | 2.59 | 3.28 |
| | $2\sigma$ spin disc. (1D) | 1.35 | 2.08 |
| | $2\sigma$ spin disc. (2D) | 1.75 | 2.53 |
| 0.1 | $5\sigma$ discovery | 3.14 | 4.39 |
| | $2\sigma$ spin disc. (1D) | 1.96 | 2.58 |
| | $2\sigma$ spin disc. (2D) | 2.28 | 2.93 |

Table 4.1: Summary of CMS reach for Randall-Sundrum gravitons.

# Chapter 5

# Summary

In the year 2008, first data in a previously unexplored energy will be available in the CMS experiment. The analysis presented above can be applied to this data, testing the possibility of new physics beyond the Standard Model. The standard muon reconstruction algorithms used in the experiment were modified to improve their performance for very energetic muons (see Section 3.3). A procedure for searching for a new heavy particle decaying into muon pairs has been proposed and described, as described in Section 4.1. Once such a particle is discovered, it's origin can be determined by analyzing angular distributions of final state muons, as has been demonstrated in Section 4.2. Possible advantages of using extra kinematic information to better distinguish a graviton from a $Z'$ were also studied.

The conclusion from the analysis is that, after collecting 100 $\text{fb}^{-1}$ of data, it is possible to discover the Randall-Sundrum graviton at $5\sigma$ level in the whole theoretically allowed region of parameter space. The reach of the experiment in graviton mass is estimated at 1.7-4.4 TeV, depending on the graviton coupling. The graviton can be distinguished from a $Z'$ particle at $2\sigma$ level for graviton masses up to 1-1.5 TeV for low coupling and 2.6-2.9 TeV for high coupling, depending on the method used.

# References


[1] Theodor Kaluza, *Zum Unitatsproblem der Physik*, Sitzungber. d. Berl. Akad. **54** (1921) 966–972. 1.1.2

[2] Oskar Klein, *Quantum Theory and Five Dimensional Theory of Relativity*, Z. Phys. **37** (1926) 895–906. 1.1.2

[3] G. Veneziano, *Construction of a crossing - symmetric, Regge behaved amplitude for linearly rising trajectories*, Nuovo. Cim. **A57** (1968) 190–197. 1.1.3

[4] Y. Nambu, *Lectures at Copenhagen Summer Symposium* (1970). 1.1.3

[5] J. Scherk and J. H. Schwarz, *Dual models for non-hadrons*, Nuclear Physics B **81** (1974) 118–144. 1.1.3

[6] T. Yoneya, *Connection of Dual Models to Electrodynamics and Gravidynamics*, Progress of Theoretical Physics **51** (1974) 1907–1920. 1.1.3

[7] John H. Schwarz, *Introduction to superstring theory* (2000). 1.1.3

[8] Nima Arkani-Hamed, Savas Dimopoulos, and G. R. Dvali, *The hierarchy problem and new dimensions at a millimeter*, Phys. Lett. **B429** (1998) 263–272. 1.2.1

[9] C. D. Hoyle et al., *Sub-millimeter tests of the gravitational inverse-square law*, Phys. Rev. **D70** (2004) 042004. 1

[10] Lisa Randall and Raman Sundrum, *Large Mass Hierarchy from a Small Extra Dimension*, Phys. Rev. Lett. **83**(17) (1999) 3370–3373. 1.2.2

[11] H. Davoudiasl, J. L. Hewett, and T. G. Rizzo, *Phenomenology of the Randall-Sundrum Gauge Hierarchy Model*, Phys. Rev. Lett. **84**(10) (2000) 2080–2083. 2, 2

[12] H. Davoudiasl, J. L. Hewett, and T. G. Rizzo, *Experimental probes of localized gravity: On and off the wall*, Phys. Rev. D **63**(7) (2001) 075004. 2, 1.1

[13] M.-C. Lemaire, V. Litvin, and H. Newman, *Search for Randall-Sundrum excitations of gravitons decaying into two photons for CMS at LHC*, CMS NOTE **2006/051** (2006). 1.3

[14] B. C. Allanach et al., *Exploring small extra dimensions at the Large Hadron Collider*, Journal of High Energy Physics **12** (2002) 039. 1.3

[15] Torbjorn Sjostrand, Leif Lonnblad, and Stephen Mrenna, *PYTHIA 6.2: Physics and manual* (2001). 1.1, 3

[16] C. Collard, M. C. Lemaire, P. Traczyk, and G. Wrochna, *Prospects for Study of Randall-Sundrum Gravitons in the CMS Experiment*, CMS NOTE **2002/050** (2002). 1.3, 3.1.1

[17] Salavat Abdoulline, A. Khanov, and N. Stepanov, *CMSJET*, CMS/TN **94-180** (1994). 1.3

[18] Sidney D. Drell and Tung-Mow Yan, *Massive Lepton-Pair Production in Hadron-Hadron Collisions at High Energies*, Phys. Rev. Lett. **25**(5) (1970) 316–320. 1.3.2

[19] David London and Jonathan L. Rosner, *EXTRA GAUGE BOSONS IN E(6)*, Phys. Rev. **D34** (1986) 1530. 1.3.2

[20] Manuel Masip and Alex Pomarol, *Effects of SM Kaluza-Klein excitations on electroweak observables*, Phys. Rev. **D60** (1999) 096005. 1.3.2

[21] Mirjam Cvetic and Paul Langacker, *New Gauge Bosons from String Models*, Mod. Phys. Lett. **A11** (1996) 1247–1262. 1.3.2

[22] Tao Han, Heather E. Logan, Bob McElrath, and Lian-Tao Wang, *Phenomenology of the little Higgs model*, Phys. Rev. **D67** (2003) 095004. 1.3.2

[23] A. Asner et al., *The Large Hadron Collider in the LEP tunnel*, CERN/AC **95-05** (1987). 2.1

[24] CMS Collaboration, *The Muon Project Technical Design Report*, CERN/LHCC **97-32** (1997), CMS TDR 3. 2.3.1

[25] Georges Charpak, G. Melchart, G. Petersen, and F. Sauli, *High accuracy localization of minimum ionizing particles using the cathode induced charge center of gravity read- out*, Nucl. Instr. Meth. **167** (1979) 455. 2.3.3

[26] M. Andlinger et al., *Pattern Comparator Trigger (PACT) for the muon system of the CMS experiment*, Nucl. Instrum. Meth. **A370** (1996) 389–395. 2.3.4

[27] CMS Collaboration, *The Tracker Project Technical Design Report*, CERN/LHCC **98-006** (1998), CMS TDR 5, Addendum CERN/LHCC 2000-016. 2.4

[28] CMS Collaboration, *The Electromagnetic Calorimeter Technical Design Report*, CERN/LHCC **97-033** (1997), CMS TDR 4, Addendum CERN/LHCC 2002-027. 2.5.1

[29] CMS Collaboration, *The Hadron Calorimeter Technical Design Report*, CERN/LHCC **97-031** (1997), CMS TDR 2. 2.5.2

[30] CMS Collaboration, *The TriDAS Project Technical Design Report, Volume 1: The Trigger Systems*, CERN/LHCC **2000-38** (2000), CMS TDR 6.1. 2.7, 2.8

[31] CMS Collaboration, *The TriDAS Project Technical Design Report, Volume 2: Data Acquisition and High-Level Trigger*, CERN/LHCC **2002-26** (2002), CMS TDR 6.2. 2.7

[32] H. L. Lai et al., *Global QCD analysis of parton structure of the nucleon: CTEQ5 parton distributions*, Eur. Phys. J. **C12** (2000) 375–392. 3

[33] OSCAR: CMS Simulation Package Home Page, `http://cmsdoc.cern.ch/oscar`. 3

[34] S. Agostinelli et al., *GEANT4: A simulation toolkit*, Nucl. Inst. and Meth. **A506** (2003) 250–303. 3

[35] ORCA: CMS Reconstruction Package, Site located at `http://cmsdoc.cern.ch/orca`. 3

[36] R. Hamberg, W. L. van Neerven, and T. Matsuura, *A Complete calculation of the order $\alpha_s^2$ correction to the Drell-Yan K-factor*, Nucl. Phys. **B359** (1991) 343–405. 3.1.2

[37] E. Gatti et al., *Analysis of the position resolution in centroid measurements in MWPC*, Nucl. Instrum. Meth. **A188** (1981) 327–346. 3.2.1.2

[38] V. Innocente, M. Maire, and E. Nagy, *GEANE: Average Tracking and Error Propagation Package*, CERN Program Library, IT-ASD W5013-E (1991). 3.2.2

[39] R. Frühwirth, *Application of Kalman Filtering to Track and Vertex Fitting*, Nucl. Instrum. and Methods **A262** (1987) 444. 3.2.2

[40] CMS Collaboration, *The CMS Physics Technical Design Report, Volume 1*, CERN/LHCC **2006-001** (2006), CMS TDR 8.1. 3.3, 3.3, 3.4

[41] G. Wrochna, *Muon Trigger of the CMS detector for LHC*, CMS NOTE **1997/096** (1997). 3.5

[42] CMS Collaboration, *The Compact Muon Solenoid Technical Proposal*, CERN/LHCC **94-38** (1994), LHCC/P1. 3.3.1

[43] V. Bartsch and G. Quast, *Expected signal observability at future experiments*, CMS NOTE **2005/004** (2005). 4.1.1

[44] R. Cousins, J. Mumford, and V. Valuev, *Detection of $Z'$ Gauge Bosons in the Dimuon Decay Mode in CMS*, CMS NOTE **2005/002** (2005). 5

[45] S. Wilks, *The Large-Sample Distribution of the Likelihood Ratio for Testing Composite Hypotheses*, The Annals of Mathematical Statistics **9** (1938) 60–62. 5

[46] J. C. Collins and D. E. Soper, *Angular distribution of dileptons in high-energy hadron collisions*, Phys. Rev. D **16** (1977) 2219–2225. 4.2

[47] Robert Cousins, Jason Mumford, Jordan Tucker, and Viatcheslav Valuev, *Spin discrimination of new heavy resonances at the LHC*, Journal of High Energy Physics **2005**(11) (2005) 046. 8

[48] J. Bijnens, P. Eerola, M. Maul, A. Mansson, and T. Sjostrand, *QCD Signatures of Narrow Graviton Resonances in Hadron Colliders*, Physics Letters B **503** (2001) 341. 4.3

[49] I. Belotelov et al., *Search for Randall-Sundrum Graviton Decay into Muon Pairs*, CMS NOTE **2006/104** (2006). 4.5